ISSN (online) 3135-4777

ABAI KAZAKH NATIONAL PEDAGOGICAL UNIVERSITY

INTERNATIONAL JOURNAL OF ADVANCED PHYSICS AND ASTRONOMY

№1 (1)

Almaty, 2026

Abai Kazakh National Pedagogical University

International Journal of Advanced Physics and Astronomy, №1 (1), 2026

Periodicity – 4 numbers in a year
Publishing from 2026.

050010, Almaty, Dostyk ave., 13
Abai Kazakh National Pedagogical University
Publishing house «Ulagat»

C o n t e n t

IRSTI 29.51.21 https://doi.org/10.51889/IJAPA.2026.1.1.001

A MINIMAL NEWTONIAN MODEL FOR WHITE DWARFS WITH DARK MATTER ADMIXTURE

A. Muratkhan[1], **N. Shynggyskhan**[1] and **S. Toktarbay**[1*]

[1] *Al-Farabi Kazakh National University, Almaty, Kazakhstan*

*Corresponding Author: saken.toktarbay@kaznu.edu.kz

Received 18 May 2026; Accepted 30 May 2026

Abstract. We consider a simple Newtonian model of a non-rotating white dwarf containing a dark-matter admixture. The baryonic component is described by the Chandrasekhar equation of state for a cold degenerate electron gas, whereas the dark component is modeled as an independent polytropic fluid. The two components are coupled only through the common Newtonian gravitational field. Numerical solutions are constructed for a reference baryonic sequence and for representative mixed configurations with fixed dark-sector parameters. Attention is restricted to three basic outputs: the density profiles, the mass–radius relation, and the limiting mass readout within the explored density interval. At $\rho_{b,c} = 10^8$ g cm^{-3}, the representative mixed models reduce the total mass by about 14.08% for $\delta = 0.25$ and by about 19.17% for $\delta = 0.35$, relative to the purely baryonic configuration. The goal is not to identify a specific dark-matter particle model, but to provide a transparent baseline calculation showing how an additional gravitating component can modify the equilibrium sequence of white dwarfs.

Keywords: white dwarfs; dark matter admixture; Newtonian gravity; Chandrasekhar equation of state; mass–radius relation.

1. INTRODUCTION

The nature of dark matter remains one of the central open problems in modern astrophysics and cosmology. Although its existence is supported by a broad range of gravitational observations, its microscopic properties are still unknown [1, 2, 3]. For this reason, compact astrophysical objects are often used as theoretical laboratories for testing whether a dark component can leave observable or structural signatures in self-gravitating systems [4, 5, 6].

Among compact stars, white dwarfs are especially suitable for baseline studies. Their equilibrium structure is well understood in Newtonian gravity through the Chandrasekhar model, where electron degeneracy pressure supports the star against gravitational collapse [7, 8, 9, 10, 11, 12]. This makes white dwarfs a natural reference system for asking a simple and physically meaningful question: how does the presence of an additional dark matter component modify the standard baryonic configuration?

Dark matter effects in compact stars have been discussed in different contexts, including neutron stars, mixed compact objects, and self-gravitating dark-sector configurations [4, 5, 6]. However, much of the existing literature is focused either on relativistic stars, on model-dependent dark-sector interactions, or on scenarios with more complicated microphysics. In contrast, there is still value in constructing a minimal and transparent Newtonian benchmark for white dwarfs with dark matter admixture. Such a model can clarify the basic structural trends, provide a clean point of comparison with the standard Chandrasekhar sequence, and serve as a starting point for later extensions. Dark-matter-admixed white dwarfs have been investigated in several related contexts [13, 14, 15, 16, 17]. Leung et al. studied white dwarfs containing degenerate fermionic dark-matter cores and showed that sufficiently light dark matter can significantly reduce the stellar radius and the Chandrasekhar mass limit [13]. More recent relativistic two-fluid studies have further demonstrated that light fermionic dark

matter may modify the compactness and radial stability properties of white dwarfs [15]. Other approaches have incorporated cold dark matter into hot-white-dwarf equations of state or have adopted a single-fluid treatment of the baryonic and dark components [17]. These works indicate that even a modest dark component can produce measurable structural changes in white-dwarf configurations.

The purpose of the present work is complementary. Instead of adopting a specific particle-physics model or a fully relativistic formulation, we construct a minimal Newtonian two-component benchmark in which the baryonic sector is described by the Chandrasekhar equation of state and the dark sector by an effective polytropic equation of state. This formulation allows us to isolate the equilibrium role of dark matter admixture, to compare directly with the standard Chandrasekhar sequence, and to distinguish the baryonic radius from the full spatial extent of the mixed configuration.

In the present work, we consider a non-rotating, spherically symmetric white dwarf containing both baryonic matter and a dark matter component. The two sectors are treated as fluids coupled through the common gravitational potential. The baryonic matter is described by the Chandrasekhar equation of state, while the dark matter component is modeled with an independent equation of state [7, 10, 12, 13].

The paper is organized as follows. Section 2. introduces the two-component model and the equations of state. Section 3. summarizes the numerical scheme and the global quantities extracted from the solutions. Section 4. presents the main results. Final remarks and limitations are collected in Section 5..

2. NEWTONIAN TWO-COMPONENT MODEL

We consider a cold, non-rotating, spherically symmetric white dwarf composed of a baryonic component and a dark matter component. Both fluids move in the same Newtonian gravitational potential. The total mass density is therefore written as

$$\rho_{tot}(r) = \rho_b(r) + \rho_{dm}(r), \tag{1}$$

where ρ_b and ρ_{dm} denote the baryonic and dark-matter densities, respectively. The enclosed total mass satisfies

$$\frac{dm}{dr} = 4\pi r^2 \left[\rho_b(r) + \rho_{dm}(r)\right]. \tag{2}$$

Hydrostatic equilibrium for the two components is then described by

$$\frac{dp_b}{dr} = -\rho_b \frac{Gm(r)}{r^2}, \tag{3}$$

$$\frac{dp_{dm}}{dr} = -\rho_{dm} \frac{Gm(r)}{r^2}. \tag{4}$$

In other words, the two fluids are coupled only through their common gravitational field. No direct non-gravitational interaction is included.

2.1. *Baryonic equation of state*

The baryonic component is described by the zero-temperature Chandrasekhar equation of state, with the standard zero-temperature electron-gas formulation and related refinements [7, 9, 18]. Introducing the relativity parameter

$$x = \frac{p_F}{m_e c}, \tag{5}$$

where p_F is the electron Fermi momentum, one can write the pressure and density as

$$p_b(x) = K\left[x(2x^2-3)\sqrt{1+x^2}+3\sinh^{-1}(x)\right], \tag{6}$$

$$\rho_b(x) = \rho_0 x^3. \tag{7}$$

The constants are

$$K = \frac{\pi m_e^4 c^5}{3h^3}, \qquad \rho_0 = \frac{8\pi\mu_e m_u (m_e c)^3}{3h^3}, \tag{8}$$

where m_e is the electron mass, m_u is the atomic mass unit, h is Planck's constant, c is the speed of light, and μ_e is the mean molecular weight per electron. In the numerical calculations we set $\mu_e = 2$, appropriate for a carbon–oxygen white dwarf.

2.2. *Dark matter equation of state*

The dark component is modeled phenomenologically as a polytropic fluid,

$$p_{dm} = K_{dm}\rho_{dm}^{\gamma}, \tag{9}$$

where K_{dm} is the polytropic constant and γ is the effective adiabatic index. Polytropic models are widely used as effective descriptions of self-gravitating fluids, including compact-star applications [19, 20, 21, 22, 23]. This form is introduced only as an effective description; it is not intended to select a unique microscopic dark-matter model.

For the numerical calculations presented here, the dark-sector parameters are fixed to

$$\gamma = \frac{5}{3}, \qquad \alpha = \frac{K_{dm}\rho_0^{\gamma}}{K} = 1. \tag{10}$$

With this choice, the dark component is represented by a single reference polytropic law whose dimensionless pressure scale is tied to the Chandrasekhar normalization. The aim of this choice is deliberately restricted: it provides a controlled setup in which the structural effect of an additional self-gravitating component can be isolated.

2.3. *Central conditions and radii*

At the center we impose

$$m(0) = 0, \qquad \rho_b(0) = \rho_{b,c}, \qquad \rho_d m(0) = \rho_{dm,c}. \tag{11}$$

The central admixture parameter is defined by

$$\delta = \frac{\rho_{dm,c}}{\rho_{b,c}}. \tag{12}$$

The limit $\delta = 0$ reduces the system to the standard baryonic white-dwarf sequence.

The baryonic radius is defined through

$$p_b(R_b) = 0, \tag{13}$$

or, equivalently, by the condition $x(R_b) = 0$. The dark-matter radius is defined by

$$p_{dm}(R_{dm}) = 0. \tag{14}$$

The total radial extent is

$$R = \max(R_b, R_{dm}). \tag{15}$$

In what follows, R_b is used as the main stellar radius because it marks the outer boundary of the visible baryonic matter.

2.4. Dimensionless equations used in the integration

For the numerical integration it is convenient to introduce the Chandrasekhar scales

$$a = \left(\frac{K}{4\pi G\rho_0^2}\right)^{1/2}, \qquad m_0 = 4\pi\rho_0 a^3, \tag{16}$$

and the dimensionless variables

$$r = a\bar{r}, \qquad m = m_0\bar{m}, \qquad \rho_b = \rho_0 x^3, \qquad \rho_{dm} = \rho_0 y. \tag{17}$$

The dimensionless dark-sector stiffness is

$$\alpha = \frac{K_{dm}\rho_0^{\gamma}}{K}. \tag{18}$$

Defining

$$\phi(x) = x(2x^2-3)\sqrt{1+x^2} + 3\sinh^{-1}(x), \tag{19}$$

the coupled system becomes

$$\frac{d\bar{m}}{d\bar{r}} = \bar{r}^2(x^3+y), \tag{20}$$

$$\frac{dx}{d\bar{r}} = -\frac{\bar{m}x^3}{\bar{r}^2}\left(\frac{d\phi}{dx}\right)^{-1}, \tag{21}$$

$$\frac{dy}{d\bar{r}} = -\frac{\bar{m}}{\alpha\gamma\bar{r}^2}y^{2-\gamma}, \qquad y > 0. \tag{22}$$

The corresponding central values are

$$x(0) = x_c = \left(\frac{\rho_{b,c}}{\rho_0}\right)^{1/3}, \qquad y(0) = \delta x_c^3, \qquad \bar{m}(0) = 0. \tag{23}$$

3. NUMERICAL SETUP

Equations (20)–(22) are integrated outward from a small radius near the center. To avoid the central coordinate singularity, the integration starts at $\bar{r} = \bar{r}_0$ with the regular leading-order expansion

$$\bar{m}(\bar{r}_0) \simeq \frac{1}{3}\left(x_c^3 + y_c\right)\bar{r}_0^3. \tag{24}$$

The variables x and y are initialized at this radius by their central values. Integration is stopped when the baryonic and dark-matter components reach the chosen surface thresholds.

The baryonic central density is varied over the interval

$$\rho_{b,c} \in [10^6, 10^{11}]\ \mathrm{g\,cm^{-3}}. \tag{25}$$

The central dark-matter admixture is sampled through the representative set

$$\delta = 0,\ 0.25,\ 0.35, \tag{26}$$

where $\delta = 0$ corresponds to the standard Chandrasekhar sequence, while $\delta = 0.25$ and $\delta = 0.35$ represent two mixed cases with visibly stronger dark-matter contributions.

For each model we extract the total mass,

$$M = m(R), \tag{27}$$

the baryonic mass,

$$M_b = 4\pi \int_0^{R_b} r^2 \rho_b(r)\, dr, \tag{28}$$

and the dark-matter mass,

$$M_{dm} = 4\pi \int_0^{R_{dm}} r^2 \rho_{dm}(r)\, dr. \tag{29}$$

The final dark-matter mass fraction is

$$f_{dm} = \frac{M_{dm}}{M}. \tag{30}$$

We also define the limiting mass within the explored interval by

$$M_{lim}(\delta) = \max_{\rho_{b,c}} M(\rho_{b,c}; \delta). \tag{31}$$

This is only an operational readout over the scanned density range. It is not interpreted here as a complete dynamical stability limit.

For the representative mixed solution used in the density-profile analysis below, the integration starts at

$$\bar{r}_0 = 10^{-8}, \tag{32}$$

with the stopping thresholds

$$x_{\rm stop} = 10^{-6}, \qquad y_{\rm stop} = 10^{-6}. \tag{33}$$

The coupled equations are solved in *Mathematica* with the adaptive "StiffnessSwitching" method. The parameters used for Figure 1 are

$$\rho_{b,c} = 10^8 \ \mathrm{g\,cm^{-3}}, \qquad \delta = 0.25, \qquad \gamma = \frac{5}{3}, \qquad \alpha = 1. \tag{34}$$

4. RESULTS AND DISCUSSION

We now turn to the minimal set of outputs needed for the present purpose: density profiles, the mass–radius relation, and the limiting readout extracted from the explored sequences.

4.1. Density profiles

The radial structure is described by

$$\rho_b(r), \qquad \rho_{dm}(r), \qquad \rho_{tot}(r) = \rho_b(r) + \rho_{dm}(r). \tag{35}$$

A representative mixed model is sufficient to show how the dark component is distributed relative to the visible stellar matter and how it contributes to the total density profile.

Figure 1 displays the normalized density profiles $\rho_b/\rho_{b,c}$, $\rho_{DM}/\rho_{DM,c}$ and $\rho_{tot}/\rho_{tot,c}$ for the representative mixed configuration with $\rho_{b,c} = 10^8$ g cm^{-3}, $\delta = 0.25$, $\gamma = 5/3$ and $\alpha = 1$. The dark component is more centrally concentrated than the baryonic one and reaches zero at a smaller radius, $R_{DM} \approx 2101.81$ km, whereas the baryonic component extends to $R_b \approx 4169.29$ km. For this model

the total mass is $M \approx 1.01421\,M_\odot$, the dark-matter mass is $M_{DM} \approx 0.09843\,M_\odot$, and the corresponding mass fraction is $f_{DM} \approx 9.71 \times 10^{-2}$. This example illustrates that the dark component forms an inner compact region, while the visible stellar size remains determined by the baryonic surface.

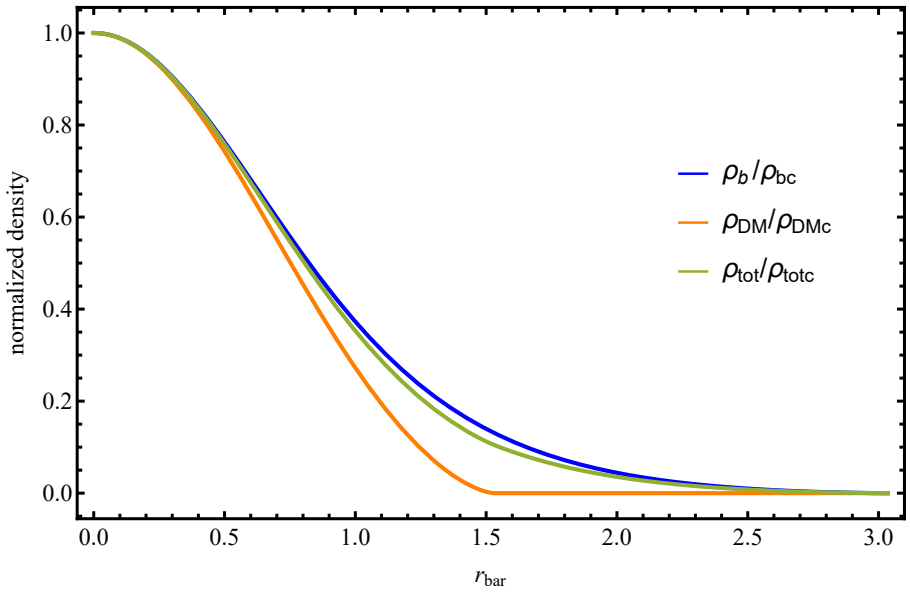

Figure 1 – Normalized density profiles $\rho_b/\rho_{b,c}$, $\rho_{DM}/\rho_{DM,c}$ and $\rho_{tot}/\rho_{tot,c}$ for the representative mixed model with $\rho_{b,c} = 10^8$ g cm^{-3}, $\delta = 0.25$, $\gamma = 5/3$ and $\alpha = 1$. The dark-matter profile decreases more rapidly with radius and terminates at $R_{DM} \approx 2101.81$ km, whereas the baryonic component extends to $R_b \approx 4169.29$ km.

4.2. Mass–radius relation

The main global quantity of interest is the mass–radius relation. In the present model the mass is the total gravitational mass obtained from Eq. (27) and the radius used for comparison is the baryonic radius R_b. Thus the relevant sequence is

$$M = M(R_b; \delta). \tag{36}$$

Figure 2 shows the mass–radius relation for the reference baryonic sequence ($\delta = 0$) together with two representative mixed cases, $\delta = 0.25$ and $\delta = 0.35$. For the mixed sequences, the numerical solutions were obtained over the central-density interval $\rho_{b,c} = 10^6$–10^8 g cm^{-3}, whereas the pure baryonic sequence was followed over the wider range $\rho_{b,c} = 10^6$–10^{11} g cm^{-3}. Within the explored interval, increasing the central dark-matter admixture shifts the mixed configurations toward lower masses and smaller baryonic radii relative to the standard Chandrasekhar sequence. This is already visible for the representative case $\rho_{b,c} = 10^8$ g cm^{-3}, where the total mass decreases from $1.18047\,M_\odot$ at $\delta = 0$ to $1.01421\,M_\odot$ at $\delta = 0.25$ and to $0.954212\,M_\odot$ at $\delta = 0.35$, while the baryonic radius decreases from 4327.58 km to 4169.29 km and 3843.33 km, respectively.

At a qualitative level, this shift is easy to understand. Once the dark component contributes to the common gravitational field, the baryonic structure responds to the total enclosed mass rather than to the baryonic mass alone. In this simple model, that is the basic mechanism behind the departure from the standard Chandrasekhar sequence.

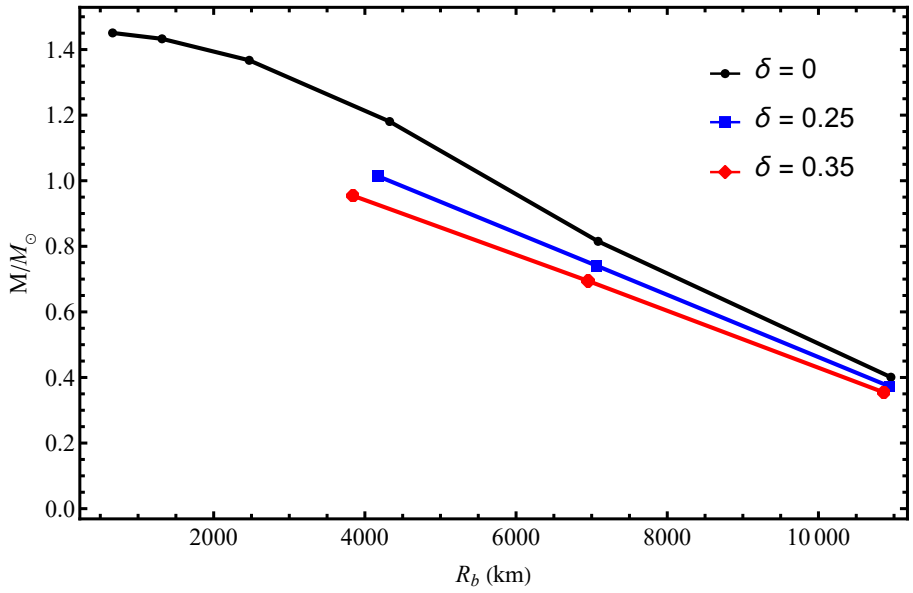

Figure 2 – Mass–radius relation $M/M_{\odot}$ versus R_b for the standard baryonic sequence ($\delta = 0$) and for two representative mixed configurations ($\delta = 0.25$ and $\delta = 0.35$). The mixed sequences are computed over the central-density range $\rho_{b,c} = 10^6$–10^8 g cm^{-3}, whereas the pure baryonic sequence extends to $\rho_{b,c} = 10^{11}$ g cm^{-3}. The mixed curves lie below the standard Chandrasekhar sequence, showing that an increasing dark-matter admixture reduces the total mass of the equilibrium configuration for the same general radius scale.

4.3. Relative impact of the dark-matter admixture

To quantify the influence of the dark component, we compare each mixed configuration with the purely baryonic model at the same central baryonic density. This comparison is useful because the parameter δ specifies only the central density ratio, whereas the final structural changes are determined by the integrated equilibrium solution. We therefore introduce the fractional changes in the total mass and in the baryonic radius as

$$\Delta M = \frac{M(\delta) - M(0)}{M(0)}, \qquad \Delta R = \frac{R_b(\delta) - R_b(0)}{R_b(0)}. \tag{37}$$

The resulting values are listed in Table 1. In the density interval where all three sequences are available, the dark-matter admixture systematically lowers the total mass and the baryonic radius. The mass reduction is already visible at $\rho_{b,c} = 10^6$ g cm^{-3} and becomes more pronounced as the central density increases. At $\rho_{b,c} = 10^8$ g cm^{-3}, the mass decreases by about 14.08% for $\delta = 0.25$ and by about 19.17% for $\delta = 0.35$. The corresponding decrease in the baryonic radius is about 3.66% and 11.19%, respectively.

This result gives a direct numerical measure of the effect of the dark component in the present minimal model. It also shows that the central admixture parameter δ should not be identified with the final dark-matter mass fraction. For example, at $\rho_{b,c} = 10^8$ g cm^{-3} the output mass fraction is $f_{DM} = 0.09705$ for $\delta = 0.25$, but it increases to $f_{DM} = 0.20760$ for $\delta = 0.35$. Thus, even for a fixed phenomenological dark-sector equation of state, the global importance of the dark component depends on the full equilibrium configuration, not only on the central input ratio.

Table 1. Relative changes of the mixed configurations with respect to the purely baryonic sequence at the same central baryonic density.

$\rho_{b,c}$ (g cm^{-3})	δ	$M/\mathrm{M}_\odot$	R_b (km)	f_{DM}	Δ_M	Δ_R
10^6	0.25	0.372661	10941.4	0.01936	-7.02%	-0.16%
10^6	0.35	0.354539	10864.5	0.03760	-11.54%	-0.86%
10^7	0.25	0.740940	7063.1	0.03330	-9.10%	-0.31%
10^7	0.35	0.694300	6953.5	0.06698	-14.82%	-1.86%
10^8	0.25	1.014210	4169.29	0.09705	-14.08%	-3.66%
10^8	0.35	0.954212	3843.33	0.20760	-19.17%	-11.19%

4.4. Limiting configurations

The largest masses obtained in the explored central-density interval are summarized through the limiting readout defined in Eq. (31). Together with the corresponding baryonic radius and dark-matter fraction, these values provide a compact comparison between the pure baryonic sequence and the representative mixed sequences.

Table 2. Limiting configurations within the explored central-density interval. For the mixed cases $\delta = 0.25$ and $\delta = 0.35$, the numerical scan was restricted to the range $\rho_{b,c} = 10^6$–10^8 g cm^{-3}. In these cases, the limiting quantities should be read as numerical outputs over the explored interval rather than as complete high-density maxima.

δ	$M_{\mathrm{lim}}/\mathrm{M}_\odot$	$R_{b,\mathrm{lim}}$ (km)	$f_{\mathrm{dm,lim}}$
0	1.45072	662.771	0
0.25	1.01421	4169.29	0.0970526
0.35	0.954212	3843.33	0.207596

The quantity f_{dm} is useful because the input parameter δ refers only to the central density ratio, whereas f_{dm} measures the final mass contribution of the dark component. In that sense, it gives a more direct estimate of how important the dark sector becomes in the resulting equilibrium configuration.

5. CONCLUSIONS

We have studied a minimal Newtonian model of a white dwarf containing a dark-matter admixture. The baryonic component was described by the Chandrasekhar equation of state, whereas the dark component was represented by an effective polytropic law. The two sectors were coupled only through the common Newtonian gravitational field. Within this deliberately restricted setup, the model provides a transparent baseline for comparing the standard Chandrasekhar sequence with mixed two-component configurations.

The numerical analysis focused on three simple but physically informative outputs: the density profiles, the mass-radius relation, and the limiting readout over the explored central-density interval. The density profiles show that, for the representative mixed configuration considered here, the dark component is more centrally concentrated than the baryonic component. The visible stellar boundary, however, remains determined by the baryonic surface.

A direct comparison at fixed central baryonic density shows that the dark-matter admixture produces a measurable reduction of both the total mass and the baryonic radius. At the reference density $\rho_{b,c} = 10^8$ g cm^{-3}, the mass decreases by about 14.08% for the case $\delta = 0.25$ and by about 19.17% for the case $\delta = 0.35$ relative to the purely baryonic configuration. The corresponding reductions in

the baryonic radius are about 3.66% and 11.19%, respectively. This result gives a direct quantitative measure of how strongly the central admixture parameter changes the global equilibrium sequence in the present model.

For the representative mixed configuration used in the density-profile analysis, we obtain $M \approx 1.01421\,M_\odot$, $R_b \approx 4169.29$ km, and $f_{DM} \approx 9.71 \times 10^{-2}$. This example illustrates that the dark component can form an inner compact region while the outer radius of the observable star is still set by the baryonic matter.

Within the explored central-density interval, increasing the central admixture from $\delta = 0$ to $\delta = 0.25$ and $\delta = 0.35$ moves the mixed configurations toward lower masses and smaller baryonic radii relative to the standard Chandrasekhar sequence. In particular, at $\rho_{b,c} = 10^8$ g cm^{-3} the total mass changes as $1.18047\,M_\odot$, $1.01421\,M_\odot$ and $0.954212\,M_\odot$ for the three cases, respectively.

The model remains intentionally limited. It does not include rotation, magnetic fields, finite-temperature corrections, general relativistic effects, or a specific microscopic dark-matter candidate. The results should therefore be interpreted as a baseline Newtonian calculation rather than as a complete astrophysical model of dark-matter-admixed white dwarfs. Nevertheless, the calculation shows that even this minimal two-component framework is able to isolate the structural role of an additional gravitating component and to quantify its impact on the white-dwarf equilibrium sequence.

REFERENCES

1. Bertone, G., D. Hooper, and J. Silk, "Particle dark matter: Evidence, candidates and constraints." 279–390, 2005.
2. Aghanim, N., Y. Akrami, M. Ashdown, J. Aumont, and C. Baccigalupi. "Planck 2018 results. vi. cosmological parameters." *Astron. Astrophys.* 641 (2020): A6. https://doi/org/10.1051/0004-6361/201833910
3. Rubin, V. C. and W. K. Ford Jr. "Rotation of the andromeda nebula from a spectroscopic survey of emission regions." *Astrophysical Journal, vol. 159, p. 379* 159 (1970): 379.
4. Bertone, G. and M. Fairbairn. "Compact stars as dark matter probes." *Physical Review D—Particles, Fields, Gravitation, and Cosmology* 77, no. 4 (2008): 043515.
5. Kouvaris, C. and P. Tinyakov. "Can neutron stars constrain dark matter?" *Physical Review D—Particles, Fields, Gravitation, and Cosmology* 82, no. 6 (2010): 063531.
6. Bramante, J. and N. Raj. "Dark matter in compact stars." *Physics Reports* 1052 (2024): 1–48.
7. Chandrasekhar, S. "The maximum mass of ideal white dwarfs." *Astrophysical Journal, vol. 74, p. 81* 74 (1931): 81.
8. Chandrasekhar, S. *An Introduction to the Study of Stellar Structure*. Chicago: University of Chicago Press, 1939.
9. Hamada, T. and E. E. Salpeter. "Models for zero-temperature stars." *The Astrophysical Journal* 134 (1961): 683–698.
10. Shapiro, S. L. and S. A. Teukolsky. *Black Holes, White Dwarfs, and Neutron Stars: The Physics of Compact Objects*. New York: Wiley-Interscience, 1983.
11. Kippenhahn, R., A. Weigert, and A. Weiss. *Stellar Structure and Evolution*. Berlin: Springer, 2013.
12. Orazymbet, A., A. Muratkhan, D. Utepova, N. Beissen, G. Baimbetova, and S. Toktarbay. "Numerical solutions and stability analysis of white dwarfs with a generalized anisotropic factor." *Galaxies* 13, no. 3 (2025): 69. https://doi.org10.3390/galaxies13030069
13. Leung, S.-C., M.-C. Chu, L.-M. Lin, and K.-W. Wong. "Dark-matter admixed white dwarfs." *Physical Review D* 87, no. 12 (2013): 123506.
14. Chan, H.-S., M.-C. Chu, and S.-C. Leung. "Dark matter-admixed rotating white dwarfs as peculiar compact objects." *The Astrophysical Journal* 941, no. 2 (2022): 115.
15. Carvalho, G. A., J. D. V. Arbañil, and J. G. Coelho. "Effects of light-mass fermionic dark matter on the equilibrium and stability of white dwarfs." *Physical Review D* 112 (2025): 044047.
16. Nunes, S. P., J. D. V. Arbañil, J. M. Z. Pretel, and S. B. Duarte. "Dark matter in white dwarfs: Implications for their structure." *Journal of High Energy Astrophysics* 50 (2026): 100505.
17. Sahoo, R., S. Mukhopadhyay, and M. Bhuyan. "Dark matter admixed white dwarfs: A single-fluid approach." *arXiv preprint arXiv:2511.17120* (2025):
18. Salpeter, E. E. "Energy and pressure of a zero-temperature plasma." *The Astrophysical Journal* 134 (1961): 669–682.

19. Horedt, G. P. *Polytropes: applications in astrophysics and related fields*. Springer, 2004.
20. Glendenning, N. K. *Compact Stars: Nuclear Physics, Particle Physics, and General Relativity*. New York: Springer, 2000.
21. Graham, P. W., R. Janish, V. Narayan, S. Rajendran, and P. Riggins. "White dwarfs as dark matter detectors." *Physical Review D* 98 (2018): 115027.
22. Bell, N. F., G. Busoni, M. E. Ramirez-Quezada, S. Robles, and M. Virgato. "Improved treatment of dark matter capture in white dwarfs." *Journal of Cosmology and Astroparticle Physics* 10 (2021): 083.
23. Hoefken Zink, J., S. Hor, and M. E. Ramirez-Quezada. "Dark matter interactions in white dwarfs: A multi-energy approach to capture mechanisms." *Journal of High Energy Physics* 05 (2025): 160.

Information about authors

Arailym Muratkhan *– PhD, Senior Lecturer, Department of Theoretical and Nuclear Physics, Al-Farabi Kazakh National University, Almaty, Kazakhstan, email: muratkhan.aray@kaznu.kz,*

Nurikamal Shynggyskhan *– PhD student of the 3rd year of the specialty «8D05306 – Physics», Department of Theoretical and Nuclear Physics, Al-Farabi Kazakh National University, Almaty, Kazakhstan, e-mail: nurkamal8503@gmail.com ,*

Saken Toktarbay *– PhD, Professor, Department of Theoretical and Nuclear Physics, Al-Farabi Kazakh National University, Almaty, Kazakhstan, e-mail: saken.toktarbay@kaznu.edu.kz.*

IRSTI 29.53.25 https://doi.org/10.51889/IJAPA.2026.1.1.002

UNIFYING THE COSMIC CARBON CYCLE: A MULTI-SCALE APPROACH TO INTERSTELLAR NANOSTRUCTURES

A.Z. Tychengulova[1*]

[1] *Abai Kazakh National Pedagogical University, Almaty, Kazakhstan*

*Corresponding Author: a.tychengulova@gmail.com

Received 18 May 2026; Accepted 6 June 2026

Abstract. Polycyclic aromatic hydrocarbons and their derivative nanostructures serve as the fundamental organic inventory of the universe. Far from static, these species undergo a complex evolutionary pathway transitioning from isolated gas-phase molecules to hybrid three-dimensional architectures, such as hydrogenated amorphous carbon and fullerenes. This mini-review reflects recent breakthroughs across observational, laboratory, and theoretical astrochemistry. With the advent of the James Webb Space Telescope, we can now resolve the fine spatial and spectral structures of photodissociation regions and distant star-forming galaxies ($z \sim 1$–2), tracking specific topological defects in carbon skeletons. Parallel to these observational milestones, laboratory action spectroscopy utilizing cryogenic ion traps has definitively linked the C_{60}^{+} cation to diffuse interstellar bands and revealed ultrafast radiative cooling mechanisms via recurrent fluorescence. On the theoretical front, we highlight the critical shift from harmonic models to anharmonic cascade emission and the deployment of *ab initio* metadynamics to simulate fullerene assembly. Finally, we explore how machine learning and neural network potentials are breaking computational bottlenecks, enabling on-the-fly kinetic modeling of amorphous dust growth.

Keywords: Polycyclic aromatic hydrocarbons (PAHs), Astrochemistry, James Webb Space Telescope (JWST), Interstellar medium (ISM), Photodissociation regions (PDRs), Cosmic dust evolution, Fullerenes, Laboratory spectroscopy, Machine learning potentials.

1. INTRODUCTION

Rather than merely serving as passive tracers of astrophysical environments, carbon nanostructures actively govern the thermodynamic and chemical balance of the interstellar medium (ISM) [1, 2, 3]. Polycyclic aromatic hydrocarbons (PAHs) dominate the photoelectric heating of neutral gas: upon absorbing energetic ultraviolet (UV) photons, they eject suprathermal electrons whose subsequent thermalization dictates the cooling rates of molecular clouds, ultimately regulating galactic star formation [4, 5, 6]. Furthermore, due to their low ionization potentials and high electron affinities, these macromolecules act as primary charge donors and acceptors, mediating the ionization equilibrium in dense media [7, 8]. Crucially, carbon dust surfaces provide the necessary catalytic substrate for molecular hydrogen (H_2) recombination, absorbing the excess bond energy while shielding fragile newly formed molecules from ambient UV fields [7, 8, 9].

The original Léger and Puget hypothesis modeled the carriers of aromatic infrared bands (AIBs) as idealized, planar gas-phase species [10, 11]. However, an influx of high-resolution spectroscopic data has forced a substantial revision of this framework [12, 13, 14]. Contemporary models invoke hybrid, heterogeneous ensembles that include hetero-substituted compounds (PANHs, PAPHs), defective lattices, and functionalized macromolecules [15, 16]. In extreme radiation environments such as photodissociation regions (PDRs), selective photodissociation destroys smaller, fragile species while leaving behind ultra-large $(N_C > 50 - 100)$ and thermodynamically resilient architectures in a survival mechanism formally recognized as the "grandPAH" concept [12]. Simultaneously, the persistent detection of broad emission continua and aliphatic features at 3.4–7.3μm has driven the adoption

of 3D amorphous network models, notably HAC [17, 18, 19, 20] and mixed aromatic/aliphatic organic nanoparticles (MAON) [21, 22, 23]. These frameworks depict highly defective, disorganized $3D$ structures where small aromatic domains are randomly linked by UV-labile aliphatic bridges [16, 24, 25].

A major paradigm shift occurred in 2010 with the detection of intense infrared emission from buckminsterfullerene (C_{60}) in the planetary nebula $Tc1$ [26]. This discovery provided compelling evidence that amorphous solid bodies can serve as direct precursors to closed-cage carbon frameworks [27, 28]. We now understand that cosmic dust formation undergoes a strict thermodynamic bifurcation, heavily dependent on the local C/O ratio and metallicity [29, 30]. The chemical buildup is a tug-of-war between "bottom-up" catalytic assembly and "top-down" photochemical degradation of larger parent bodies [31, 32]. Laboratory plasma simulations reveal that while high hydrogen partial pressures stabilize classic $2D$ planar aromatic sheets, the presence of oxygen acts as a potent steric trigger [33, 34]. Even without incorporating into the final lattice, oxygen inhibits the formation of stable six-membered rings, thereby promoting pentagon integration and forcing the carbon network to curl into $3D$ fullerenes and nano-onions [35, 36]. Consequently, the emission profiles we observe across the universe capture a dynamic carbon cycle, constantly balancing between $2D$ planar configurations and highly defective curved surfaces [29, 37, 38].

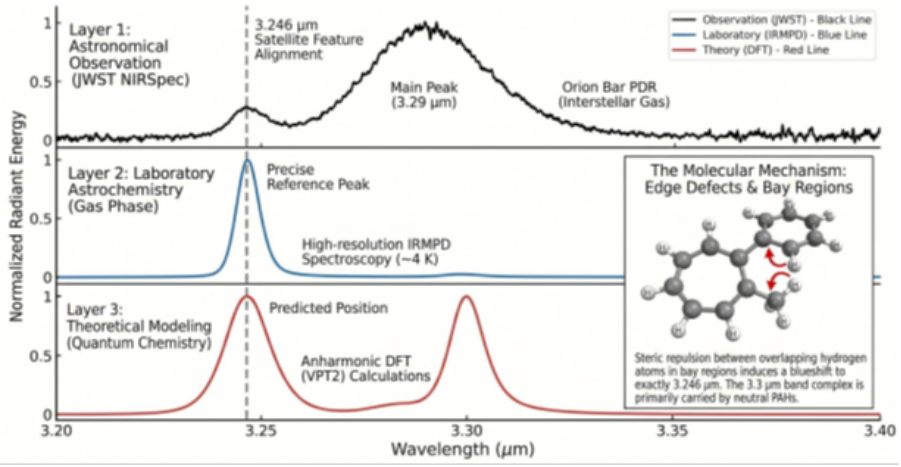

Figure 1 – Multi-layer spectral alignment of the $3.3\mu m$ PAH band complex and its $3.246\mu m$ satellite feature. The inset demonstrates the molecular mechanism where steric repulsion between overlapping hydrogen atoms in the bay regions of edge-defective neutral PAHs drives the precise blueshift to exactly $3.246\mu m$. Original infographic compiled by the author. The theoretical anharmonic $(VPT2)$ reference data are adapted from [47] and laboratory spectra as well as the JWST observational spectra are adapted from [7] focusing on $3.3\mu m$ feature.

2. Key Scientific Advances

2.1. Observational Foundations: PAH Dynamics from Local PDRs to Cosmological Scales

The commissioning of the James Webb Space Telescope (JWST) has fundamentally transformed our observational approach to *PAHs*, pushing the field past qualitative morphological classifications into the realm of precision molecular topology [39, 40]. By leveraging the unprecedented spatial and spectral resolution of the NIRSpec and MIRI instruments, recent surveys of prototypical *PDRs* like the Orion Bar have resolved the fine structure of the 3.3 μm stretching band [41, 42]. Far from a simple Gaussian profile, this feature exhibits a pronounced blue wing and a distinct satellite peak at

3.246 μm [43, 44]. Theoretical models confirm that these subtle spectral signatures arise directly from steric repulsion between hydrogen atoms nestled in the "bay regions" of edge-defective PAHs [43, 45, 46]. This remarkable empirical and computational convergence is clearly mapped in Figure 1., which demonstrates the precise alignment of the 3.246 μm satellite feature across astronomical observations, laboratory action spectroscopy, and quantum chemical simulations.

Similarly, the asymmetric blue wing of the 6.2 μm stretching band long considered a definitive marker for nitrogen-substituted PANHs is now elegantly explained by the presence of trio-H structural defects on PAH cations, removing the strict necessity for heteroatom inclusion [47, 48]. Spatially resolved emission maps across PDRs offer compelling empirical validation for the "grandPAH" hypothesis [12]. As one moves toward the irradiating stellar source, the harsh ultraviolet environment selectively obliterates smaller, fragile PAHs and strips away aliphatic side chains. Consequently, the surviving emission originates almost exclusively from population of ultra-large ($N_C > 50$–100), highly ionized, and thermodynamically resilient macromolecules [12] as illustrated in Figure 2.

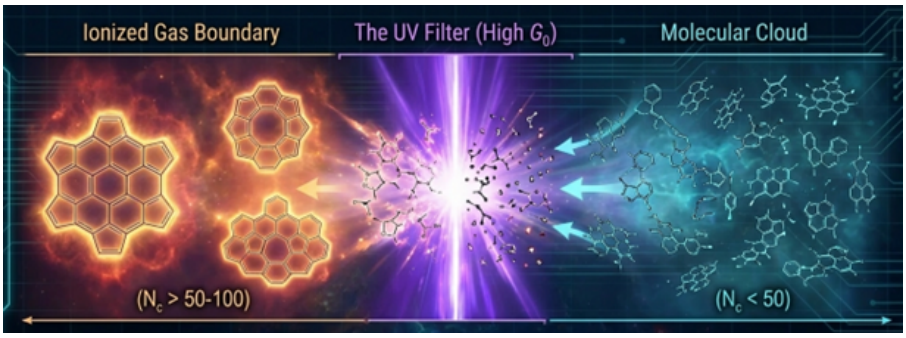

Figure 2 – Spatial architecture of the grandPAH hypothesis across a prototypical photodissociation region (PDR). Original infographic compiled by the author.

To quantitatively decode these physical environments, astronomers rely on calibrated infrared band ratios. The 11.3 μm / 7.7 μm ratio serves as a robust ionization proxy; transitioning a PAH to a cationic state amplifies the stretching dipole moments (at 6.2 μm and 7.7 μm) by an order of magnitude, while leaving the out-of-plane bending modes (11.3 μm) largely unperturbed. Concurrently, the 11.3 μm / 3.3 μm ratio acts as a sensitive molecular size (N_C) chronometer, dictated by the heat capacity and subsequent energy cascade of the UV-pumped molecule [12]. Moreover, JWST has recently extended local diagnostic frameworks to cosmological scales. Observations using the MIRI Low Resolution Spectrometer (LRS) have successfully detected PAH emission in luminous infrared galaxies (LIRGs) at redshifts of $z \sim 1$–2 [4, 49]. The 3.3 μm band luminosity has proven to be a reliable tracer of dust-obscured star formation rates (SFR), adhering to a strict linear correlation:

$$\log(L_{3.3}) = 1.07 \cdot \log(L_{\mathrm{IR}}) - 3.4 \tag{1}$$

Perhaps the most striking cosmological finding is that the mean 11.3 μm/3.3 μm ratio in these early-universe galaxies is approximately three times higher than that observed in local LIRGs [50]. This stark contrast unequivocally points to a fundamental shift in the dust size distribution at high redshifts, heavily skewed toward larger PAH grains, likely driven by enhanced coagulation rates within denser, colder gas reservoirs [4, 50]. Parallel investigations have mapped the severe survival limits of carbon nanostructures within the extreme environments of active galactic nuclei (AGN) [4, 51, 52]. The fierce X-ray radiation emanating from accretion disks systematically destroys smaller and ionized PAHs, severely suppressing the 3.3, 6.2, and 7.7 μm emission bands within the central parsecs of Seyfert galaxies [52, 53, 54, 55]. As a result, the infrared spectra of AGN-dominated systems are

sculpted entirely by an anomalous, heavily shielded population of large, neutral PAHs [56]. This selective destruction demands rigorous spectral decomposition when attempting to utilize PAHs as universal SFR indicators in active galaxies [56, 57].

2.2. Laboratory Astrochemistry: From Action Spectroscopy to Prebiotic Ice Synthesis

For decades, the interpretation of astronomical spectra relied heavily on matrix isolation techniques. While foundational, isolating molecules in cryogenic argon or neon lattices inherently corrupts intrinsic vibrational signatures via unpredictable matrix shifts and symmetry distortions [58, 59]. To bypass these solid-state artifacts, modern laboratory astrochemistry has pivoted to gas-phase "action spectroscopy," an approach that faithfully replicates the pristine vacuum of the interstellar medium [60, 61, 62]. Utilizing infrared multiple photon dissociation (IRMPD) coupled with free-electron lasers like FELIX, researchers can now track *in situ* molecular growth [60]. A prime example is the bottom-up synthesis of nitrogen-substituted $PAHs (PANHs)$ inside cryogenic ion traps. By exposing trapped pyridine cations (CH_5N^+) to acetylene (C_2H_2) at 150 K, experiments successfully mapped the stepwise polymerization leading to the endoskeletal quinolizinium core [63].

Perhaps the most historic spectroscopic triumph of the last decade involved identifying the elusive carriers of the diffuse interstellar bands $(DIBs)$. Solving this century-old enigma required cooling target ions near absolute zero without perturbing their electronic structures. Messenger spectroscopy inside superfluid helium nanodroplets $(T < 1"K")$ provided the exact methodology needed, delivering unequivocal proof that the buckminsterfullerene cation is responsible for at least two intense near-infrared DIBs at 9577 Å and 9632 Å [64, 65].

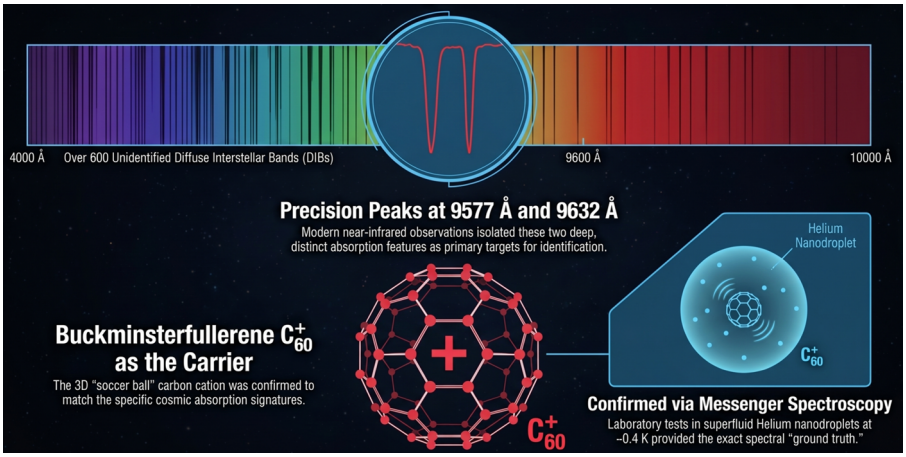

Figure 3 – Experimental identification of the buckminsterfullerene C_{60}^+ cation as a DIB carrier. Original infographic compiled by the author.

Simultaneously, the survival dynamics of PAH cations in harsh UV environments were fundamentally rewritten by experiments conducted in cryogenic electrostatic storage rings, such as the Double ElectroStatic Ion Ring Experiment (DESIREE, 13 K, $\approx 1 \times 10^{-14}$ mbar) [66, 67]. By monitoring the delayed unimolecular decay of circulating ions, physicists confirmed the existence of ultrafast recurrent fluorescence (RF), occasionally termed Poincaré fluorescence [67]. As systematically diagrammed in Figure 4., fast radiative cooling governs the stabilization of energized species, allowing highly excited PAH cations to undergo inverse internal conversion (IIC) from their vibrational ground state $(S_0^{v>0})$ into low-lying electronic excited states S_1, subsequently emitting optical or UV photons [66]. Incorporating a functional cyano group into the aromatic ring drastically lowers the energy threshold, accelerating the RF cooling rate beyond 400 s^{-1}. This exceptional photostability perfectly

explains the anomalous radio-astronomical detection of intact cyanonaphthalenes within the frigid dark core of TMC-1 [66, 68].

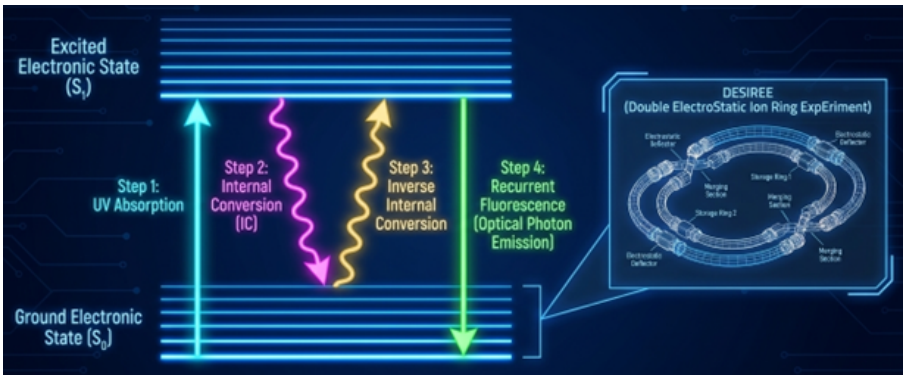

Figure 4 – Intramolecular energy cascade of recurrent fluorescence (RF) as a PAH survival mechanism. The Jablonski diagram charts the four-step cooling pathway: UV absorption, internal conversion (IC), inverse internal conversion, and subsequent optical photon emission. The inset illustrates the DESIREE storage ring layout used to observe these long-lived decay dynamics in ultra-high vacuum conditions free of collisional quenching. Original infographic compiled by the author.

Replicating the dust-forming zones of Asymptotic Giant Branch (AGB) stars requires sophisticated plasma jet reactors (COSmIC) and chambers with controlled thermal gradients (Stardust) [69]. Studies utilizing these interstellar dust analogues (IDAs) have uncovered a strict chemical bifurcation dictated by the local carbon-to-oxygen ratio. Under highly carbon-rich conditions ($C/O > 1$), molecular assembly overwhelmingly favors flat, $2D$ planar aromatic sheets [37]. Conversely, lowering the ratio to 1.1 forces oxygen to act as a steric controller; even without incorporating into the final macromolecular lattice, oxygen impedes the formation of stable hexamers. This forces the integration of pentagonal rings and aliphatic bridges, violently curling the carbon network into 3D fullerenes and highly defective mixed aromatic/aliphatic organic nanoparticles (MAONs) [37]. Providing a competing "top-down" molecular source, experiments have also demonstrated that atomic hydrogen bombardment induces graphene etching on SiC cores, actively stripping away free PAH molecules into the gas phase [37].

Finally, at 10 K, dust grains acquire thick ice mantles (H_2O, CO, CO_2, CH_3OH) that function as formidable catalytic nanoreactors. Vacuum UV irradiation ($h\nu \leq 10.2$ eV) of these ices triggers non-thermal photochemidesorption alongside the Desorption-Induced Electronic Transitions (DIET) mechanism [70, 71]. Critically, the stepwise photochemical dehydrogenation of frozen methanol yields highly reactive formaldehyde, triggering a cascade of radical-driven organic synthesis [72, 73]:

$$CH_3OH \xrightarrow{h\nu} H_2CO + 2H^{\bullet} \tag{2}$$

Simultaneously, this radiation induces the cleavage of molecular bonds, generating a high concentration of reactive intermediates, such as the hydroxymethyl ($\cdot CH_2OH$), methoxy ($\cdot OCH_3$), and hydroxyl ($\cdot OH$) radicals. The subsequent recombination of these radicals within the catalytic ice matrix ultimately yields a diverse inventory of complex organic molecules (COMs).

High-performance chromatographic analysis of the refractory residues remaining after ice sublimation has consistently confirmed the in situ generation of complex prebiotic inventories [74, 75]. These include racemic mixtures of up to 16 distinct amino acids (e.g., glycine, serine), ribose sugars, uracil, and hexamethylenetetramine (HMT) proving definitively that the fundamental chemical

building blocks of life are forged in the deep interstellar medium long before their delivery to protoplanetary disks [74, 75].

2.3. Theoretical Advancements in Astrochemistry and Molecular Dynamics

To decode the unprecedented data streams flowing from JWST and ALMA, theoretical astrophysics has decisively abandoned rudimentary harmonic approximations in favor of rigorous anharmonic modeling and machine learning integration [76, 77]. Historically tethered to modest basis sets, the field now mandates extended frameworks incorporating polarization functions (e.g., cc-pVTZ) to accurately capture the dynamic charge redistribution inherent to stretching modes [44, 47]. Furthermore, because the photophysics of vacuum-isolated PAHs is strictly governed by anharmonic cascade cooling, theorists have widely implemented second-order vibrational perturbation theory (VPT2) [78]. By computing quartic force fields (QFF) via explicitly correlated wavefunctions (F12-TZ-cCR), these advanced models successfully reproduce the critical red-shifting and asymmetric broadening of emission lines triggered by thermal relaxation [79].

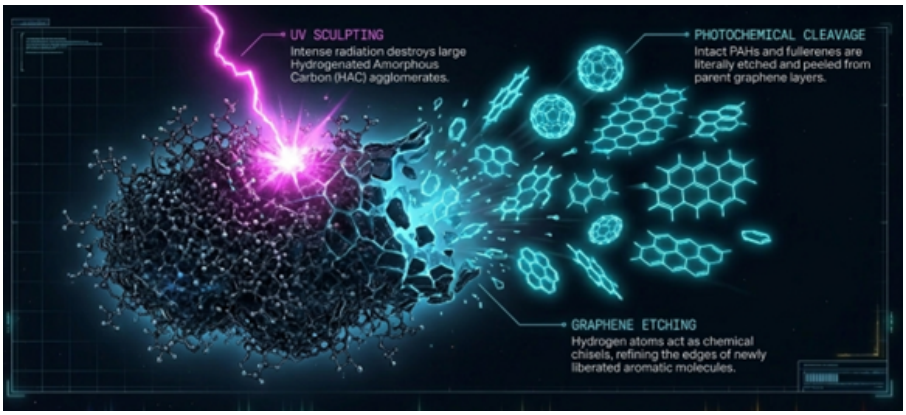

(a) Panel A

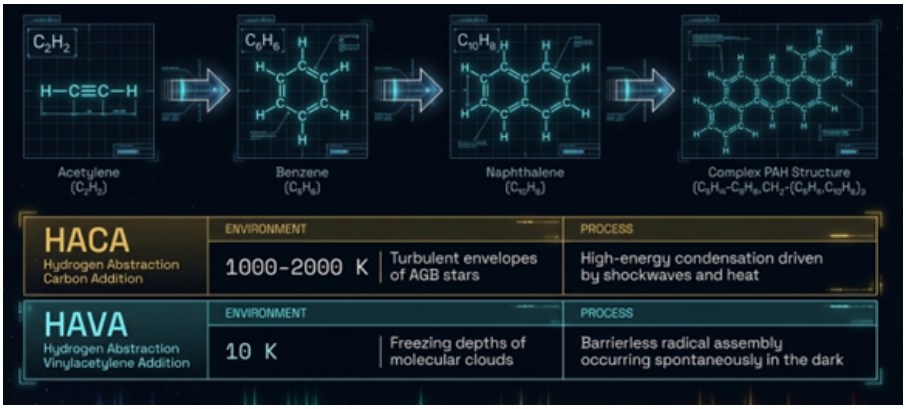

(b) Panel B

Figure 5 – Theoretical models of complementary chemical pathways in cosmic carbon evolution. Panel A (Left): Computational pathways for bottom-up PAH synthesis. Panel B (Right): Conceptual mechanics of top-down aromatization under intense stellar radiation fields. Original infographic compiled by the author.

Quantum topological analysis has definitively proven that structural anomalies at the molecular periphery drive the most perplexing spectral signatures [47]. Extensive simulations of highly defective isomers reveal that steric repulsion between hydrogen atoms nestled within "bay regions," coupled with trio-H configurations, violently blue-shifts the short-wavelength modes to 6.15 μm and

generates the distinct 3.246 μm satellite band recently observed in the Orion Bar [14, 62]. Crucially, this topological framework seamlessly explains the asymmetric blue wing of the 6.2 μm feature utilizing purely hydrocarbon cations, effectively negating the historical absolute necessity for nitrogen-substituted PANHs [44].

A pivotal theoretical advancement in molecular dynamics for astrochemistry is the application of ab initio metadynamics to overcome the severe timescale limitations of simulating low-temperature carbon evolution. In standard molecular dynamics, cold carbon nanostructures easily become kinetically trapped in deep local free-energy minima, making the observation of slow structural rearrangements computationally prohibitive. Metadynamics resolves this by introducing a history-dependent bias potential that continuously deposits artificial "penalty hills"– typically repulsive Gaussian potentials – along selected collective variables. This mechanism dynamically fills the underlying free-energy wells, physically forcing the system to cross high activation barriers without revisiting previously sampled atomic configurations. For PAH science, this accelerated exploration of the potential energy surface is transformative; it enables the efficient simulation of rare kinetic events, such as the spontaneous topological self-assembly of 2D carbon networks into 3D fullerene-like nanoparticles, capturing structural transitions that would otherwise require millions of years to unfold in the cold interstellar medium.

Simulating the high-energy "bottom-up" assembly of 3D dust grains from chaotic gas-phase pools requires pushing molecular dynamics past traditional thermodynamic barriers [7]. Because standard molecular dynamics leaves cold carbon systems kinetically trapped in deep free-energy minima, observing slow structural transitions is normally computationally prohibitive. Ab initio metadynamics (BOMD+MTD) resolves this timescale limitation by injecting a history-dependent bias constructed as a sum of repulsive Gaussian potentials or artificial "penalty hills" into the collective variable space. This mechanism dynamically fills the underlying free-energy wells, forcing the system to escape local minima and cross high activation barriers. Computational experiments conducted at 400 K demonstrate that this accelerated exploration allows flat, 2D polycyclic networks to spontaneously reorganize into low-symmetry 3D fullerene-like spheres, utilizing integrated pentagons and heptagons as essential curvature-inducing defects [7]. This kinetic balance between structural growth and degradation is theoretically and conceptually mapped in Figure 5, which contrasts the multi-regime pathways of bottom-up molecular assembly (Panel A) against the radiation-driven mechanisms of top-down macromolecular erosion (Panel B) within interstellar environments.

At the solid-state interface, hybrid QM/MM schemes have completely redefined our understanding of catalytic ice mantles [80]. Modeling the surface adsorption of *trans*-glycine and highly polar radicals onto water clusters reveals a massive reconfiguration of hydrogen bond networks (1.46–2.53 Å) [80]. This interaction yields staggering binding energies ($B.E.$): $B.E.(\textit{trans}\text{–glycine}) \approx$ 11670 K, $B.E.(\mathrm{COOH}^{\bullet}) > 10000$ K [80, 81]. Such extreme surface fixation completely paralyzes radical diffusion, imposing severe kinetic bottlenecks on classical Langmuir-Hinshelwood surface reactions. Conversely, quantum models probing the limits of structural resilience have uncovered an immense Ionization Tolerance Limit (ITL) for closed carbon cages; the fullerene can endure macroscopic charging up to C_{60}^{26+} under intense X-ray irradiation before ultimately succumbing to Coulomb explosion [82].

Finally, the integration of machine learning (ML) is systematically eradicating the computational bottleneck inherent to quantum mechanics [83]. Random Forest algorithms, trained on Morgan fingerprints derived from over 14,000 PAH structures, can now predict infrared responses with microsecond latency [84]. Perhaps the most profound theoretical breakthrough involves modeling the on-the-fly kinetic growth of hydrogenated amorphous carbon (α–C) using neural network interatomic poten-

tials (MLPs) [85, 86]. To cure the physical "shortsightedness" of standard MLPs which typically utilize a restrictive 5–8 Å cutoff radius, developers are deploying Message-Passing Neural Networks (MPNNs) that successfully capture long-range π-electron delocalization across the macromolecule [87]. Complementing these neural architectures, modern graph theory provides a remarkably robust analytical invariant: the total number of perfect matchings (Kekulé structures) within the modified planar graphs of hydrogenated fullerenes (e.g., $C_{60}H_2$) maintains a strict negative correlation with quantum thermodynamic energy, permitting the instantaneous topological screening of millions of candidate isomers [88].

3. Critical Analysis of Current Gaps: Kinetic Paradoxes and Spectroscopic Dark Matter

Despite the recent triumphs in high-resolution infrared astronomy and computational quantum chemistry, the evolutionary paradigm of PAHs confronts severe kinetic and spectroscopic inconsistencies. Transitioning this field from a phenomenological framework to a rigorous predictive science requires resolving four fundamental paradoxes.

3.1. The Cold Core Paradox and the Collapse of HACA

Historically, infrared astronomy suffered from a critical limitation: AIBs trace the vibrational modes of entire structural classes rather than individual molecular species [12, 13]. Radio astronomy recently shattered this barrier. By deploying spectral matched filtering algorithms on Green Bank Telescope data (the GOTHAM survey), astronomers successfully mapped rotational transitions of specific polar macromolecules such as 1-cyanonaphthalene, indene, and the four-ring 1-cyanopyrene ($C_{16}H_9CN$) deep within the frigid molecular cloud TMC-1 [62]. However, the observed column densities of these species at temperatures near 10 K wildly exceed the predictions generated by classical high-temperature astrochemical networks. The standard "bottom-up" Hydrogen Abstraction Carbon Addition (HACA) mechanism is thermodynamically paralyzed in such cold environments [89]. This glaring discrepancy forces a paradigm shift toward barrierless, radical-driven pathways, such as Hydrogen Abstraction Vinylacetylene Addition (HAVA), to explain the synthesis of complex rings in dark clouds [90].

3.2. Ice Mantles as Kinetic Traps

Deep within dense clouds, carbonaceous dust grains accrete thick ice mantles primarily composed of H_2O, CO, and NH_3, transforming into catalytic nanoreactors [91]. A major theoretical void exists in accurately modeling the binding energies (B.E.) of polar intermediates at this solid-state interface. Advanced QM/MM simulations demonstrate that the formation of dense hydrogen-bond networks radically alters molecular conformations and violently elevates binding energies [7]. For highly polar species, such as the hydroxymethyl ($\cdot CH_2OH$) radical, surface fixation becomes extreme:

$$\text{B.E.}(\text{COOH}^{\bullet}) \approx 8000\,\text{K to } 11000\,\text{K} \tag{3}$$

This profound immobilization completely paralyzes thermal surface diffusion, fatally crippling classical Langmuir-Hinshelwood catalytic models. Consequently, returning intact macromolecules to the gas phase bypasses thermal desorption entirely, necessitating non-thermal triggers such as heavy-ion cosmic ray bombardment [92].

Unlike thermal processes governed by the cold bulk temperature of the ice, heavy cosmic ray ions overcome massive thermodynamic bottlenecks through direct energy transfer. As these highly

energetic particles traverse the icy dust mantles, their high electronic energy loss deposits massive amounts of energy locally along their trajectory. This interaction creates ionization tracks and localized "thermal spikes" that instantaneously exceed the surface fixation binding energies. Such extreme, non-thermal energy deposition disrupts the local hydrogen-bond networks, simultaneously triggering complex radiolysis within the ice and driving the nonthermal desorption of intact macromolecules back into the gas phase without fragmentation.

3.3. DIBs, ERE, and Spectroscopic "Dark Matter"

While cryogenic messenger spectroscopy brilliantly secured the C_{60}^+ cation as the definitive carrier of the 9577 Å and 9632 Å diffuse interstellar bands (DIBs), the molecular identities behind over 600 optical and 60 near-infrared DIBs remain elusive [93, 94]. Hypotheses invoking specific ultra-large PAH cations face an acute deficit of isolated gas-phase laboratory data. The spectroscopic puzzle is further complicated by "C_2-DIBs" bands exhibiting unresolved rotational branches that imply carrier molecules of vastly different masses [95]. Intrinsically linked to this "dark matter" problem is the Extended Red Emission (ERE), a broad photoluminescent continuum spanning 500 nm–900 nm. Candidates ranging from oxygen-functionalized PAHs (OPAHs) to carbon nanodots have been proposed, yet a rigorous energy-conversion mechanism seamlessly linking UV photon absorption to this red luminescence remains conspicuously absent [96].

3.4. Survival Thresholds in These Extreme Environments

The extreme environments of Seyfert galaxies and quasars shatter standard observational calibrations. The fierce X-ray radiation and shockwaves emanating from supermassive black hole accretion disks systematically annihilate small and ionized PAHs, severely suppressing the 3.3 μm, 6.2 μm, and 7.7 μm emission features [53]. Consequently, the infrared spectra of AGN-dominated systems are sculpted entirely by an anomalous, heavily shielded population of ultra-large ($N_C > 300 - 400$), predominantly neutral PAHs [97]. How these neutral macromolecules evade catastrophic Coulomb explosions at distances of 10–500 from the nucleus remains fiercely debated, with dense molecular tori frequently invoked as the likely shielding mechanism. Ultimately, this selective destruction renders the uncorrected use of PAH luminosities as universal star formation rate (SFR) indicators highly perilous in active galaxies, demanding rigorous spectral decomposition [53, 98].

4. FUTURE FRONTIERS: TOWARD PREDICTIVE MULTI-SCALE FRAMEWORKS

Resolving the lingering kinetic and spectroscopic inconsistencies within astrochemistry demands transitioning from isolated quantum models to predictive, multi-scale frameworks. The next decade will be defined by the tight integration of machine learning (ML), ultra-sensitive radio astronomy, and cryogenic surface physics.

4.1. On-the-Fly Machine Learning and Topological Screening

Overcoming the $\mathcal{O}(N^3)$ computational bottleneck inherent to Density Functional Theory (DFT) relies heavily on deploying MLPs. Modeling the kinetic growth of highly disordered phases, such as hydrogenated amorphous carbon (α–C) and MAONs, on-the-fly requires bypassing the physical shortsightedness of standard models, which typically utilize restrictive 5 Å–8 Å cutoff radii. MPNNs resolve this limitation by successfully capturing long-range π-electron delocalization across extensive macromolecular networks [87].

Furthermore, graph theory drastically accelerates thermodynamic screening: the total number of

Kekulé structures within modified planar graphs of hydrogenated fullerenes (e.g., $C_{60}H_2$) maintains a strict negative correlation with actual quantum thermodynamic energy. This mathematical invariant permits the instantaneous topological filtering of millions of structural isomers without executing resource-intensive *ab initio* calculations [88].

4.2. Multi-Wavelength Synergy: Cross-Correlating ALMA and JWST

Shattering the profound spectral degeneracy of AIBs demands cross-correlating mid-infrared vibrational data with sub-millimeter rotational spectroscopy (ALMA, GBT). The recent success of spectral matched filtering within the GOTHAM survey which definitively identified polar macromolecules like 1-cyanopyrene inside the frigid TMC-1 cloud paves the way for true single-molecule tomography.

Superimposing JWST infrared continuum maps onto ALMA kinematic maps of specific cyano-PAHs will definitively resolve the lingering "grandPAH" versus "multi-PAH" debate. Simultaneously, this multi-wavelength synergy provides the only observational avenue to validate barrierless, radical-driven growth mechanisms, such as HAVA operating near 10 K.

4.3. Quantum Astrochemistry of Cryogenic Ice Nanoreactors

Precision modeling of interfacial catalysis across the dust-ice boundary constitutes the third strategic frontier. Advancing hybrid QM/MM schemes is imperative for accurately predicting the staggering binding energies of polar radicals trapped on and ice mantles. Future computational frameworks must accurately calculate non-thermal desorption cross-sections triggered by heavy-ion cosmic rays, operating alongside UV-driven DIET.

Mapping these radical-driven photochemical cascades will finally close the gap in understanding the deep-space synthesis of prebiotic inventories, ranging from racemic amino acids to HMT. Furthermore, quantifying the exact contribution of ultra-large gas-phase macromolecules (e.g., ovalene) to the surface catalysis of molecular hydrogen remains critical for accurately modeling the cooling rates of dense photodissociation regions.

5. CONCLUSION

Over the past decades, the cosmic carbon paradigm has evolved dramatically from the idealized Léger and Puget hypothesis of isolated, planar PAHs to a comprehensive, continuous evolutionary cycle. We now recognize that two-dimensional aromatic sheets, highly defective 3D networks (HAC, MAON), and closed-cage fullerenes exist in a dynamic thermodynamic equilibrium dictated by radiation fields, metallicity, and coagulation kinetics.

This grand evolutionary narrative is comprehensively synthesized in the concluding diagram on Figure 6, which maps the entire cosmic journey of carbonaceous matter spanning stardust injection from AGB stars, competitive bottom-up and top-down processing tracks, molecular freeze-out onto cryogenic ice mantles, and the subsequent radical-driven synthesis of life's building blocks delivered directly to young planetary systems.

The synchronized leaps in observational and laboratory astrophysics have cemented this unified framework. JWST surveys, notably the ERS PDRs4All program, have conclusively mapped the topological markers of edge defects proving that steric interactions drive the 3.3 μm blue wing and the 6.2 μm asymmetry, thereby eliminating the absolute necessity for nitrogen-substituted PANHs. Cosmologically, these frameworks have established rigorous PAH-based SFR calibrations in highly obscured, high-redshift ($z \sim 1$–2) environments, while revealing that severe X-ray destruction in AGN aggressively shifts the surviving molecular distribution toward ultra-large, neutral species.

Simultaneously, cryogenic action spectroscopy has resolved century-old enigmas, securing the

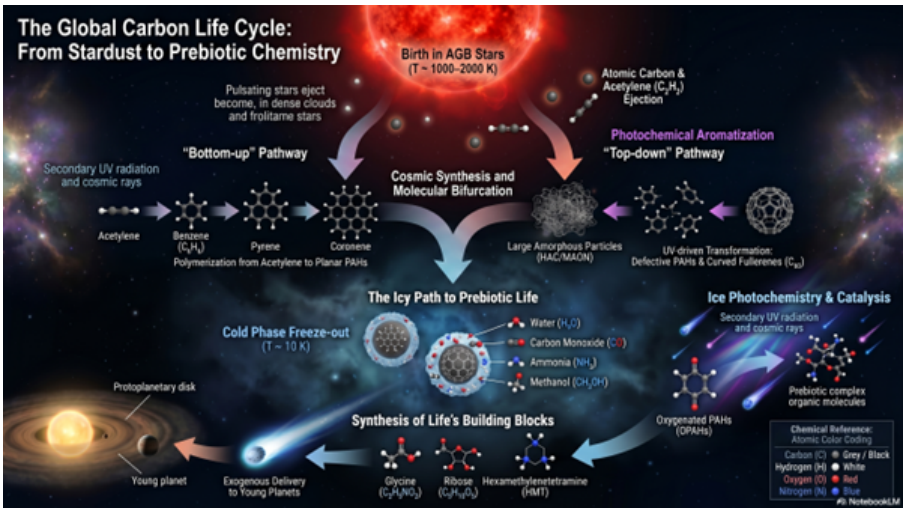

Figure 6 – Comprehensive scheme of the global cosmic carbon lifecycle from stardust production to prebiotic chemistry. Original infographic developed by the author; visualization is based on the author's initial framework and rendered utilizing the Nano Banana Pro AI tool.

cation as a definitive DIB carrier and exposing the ultrafast radiative cooling of functionalized PAHs via recurrent fluorescence. Theoretical modeling has matched this pace, shifting from rigid harmonic approximations to fully anharmonic cascade emission models and utilizing *ab initio* metadynamics to simulate bottom-up fullerene assembly.

Moving forward, deciphering the remaining hundreds of unassigned DIBs, untangling prebiotic ice catalysis, and mapping extreme AGN survival thresholds depends entirely on interdisciplinary synthesis. Fusing multi-wavelength spectroscopy with machine-learning-accelerated quantum dynamics will definitively elevate carbon nanostructures from passive spectroscopic tracers to the primary thermodynamic architects of the baryonic universe.

ACKNOWLEDGMENTS

This work was supported by Abai Kazakh National Pedagogical University within the framework of the Postdoctoral Research Fellowship Program.

REFERENCES

[1] Watson, W. D. and E. E. Salpeter. "Molecule formation on interstellar grains." *The Astrophysical Journal* 174 (1972): 321–340.

[2] Helou, G., S. Malhotra, D. J. Hollenbach, D. A. Dale, and A. Contursi. "Evidence for the Heating of Atomic Interstellar Gas by Polycyclic Aromatic Hydrocarbons." 548, no. 1 (2001): L73–L76.

[3] Soliman, N. H., P. F. Hopkins, and M. Y. Grudić. "Thermodynamics of giant molecular clouds: The effects of dust grain size." *The Astrophysical Journal* 975 (2024): 284–295.

[4] McKinney, J. *et al.* "A JWST MIRI LRS survey of 37 massive star-forming galaxies and active galactic nuclei at cosmic noon: Overview and first results." *The Astrophysical Journal* 1001 (2026): 93–109.

[5] Traina, A. *et al.* "A3COSMOS: The infrared luminosity function and dust-obscured star formation rate density at $0.5 < z < 6$." *Astronomy & Astrophysics* 681 (2024): A118–A130.

[6] Zavala, J. A. *et al.* "The evolution of the IR luminosity function and dust-obscured star formation over the past 13 billion years." *The Astrophysical Journal* 909 (2021): 165–180.

[7] Hansen, K., D. García-Hernández, E. Campbell, D. Erbahar, A. Domaracka, C. Jäger, C. Ewels, P. Umek, S. Kwok, and E. Peeters. "Roadmap on carbon molecular nanostructures in space." *The European Physical Journal D* 79 (2025): 94–105.

[8] Kwok, S. and Y. Zhang. “Mixed aromatic–aliphatic organic nanoparticles as carriers of unidentified infrared emission features.” *Nature* 479 (2011): 80–83.

[9] Kwok, S. “The mystery of unidentified infrared emission bands.” 367, no. 2 (2022): 16.

[10] Puget, J. and A. Léger. “A new component of the interstellar matter-small grains and large aromatic molecules.” *Annual Review of Astronomy and Astrophysics* 27 (1989): 161–198.

[11] Allamandola, L., A. Tielens, and J. Barker. “Interstellar polycyclic aromatic hydrocarbons-the infrared emission bands, the excitation/emission mechanism, and the astrophysical implications.” *Astrophysical Journal Supplement Series* 71 (1989): 733–775.

[12] Andrews, H., C. Boersma, M. Werner, J. Livingston, L. Allamandola, and A. Tielens. “PAH emission at the bright locations of PDRs: The grandPAH hypothesis.” *The Astrophysical Journal* 807 (2015): 99–114.

[13] Rosenberg, M. J., O. Berné, and C. Boersma. “Random mixtures of polycyclic aromatic hydrocarbon spectra match interstellar infrared emission.” *Astronomy & Astrophysics* 566 (2014): L4–L13.

[14] Boersma, C., J. Bregman, and L. J. Allamandola. “The charge state of polycyclic aromatic hydrocarbons across a reflection nebula, an H II region, and a planetary nebula.” *The Astrophysical Journal* 858 (2018): 67.

[15] Peeters, E. “The PAH hypothesis after 25 years.” *Proceedings of the International Astronomical Union* 7 (2011): 149–161.

[16] Peeters, E., C. Mackie, A. Candian, and A. G. Tielens. “A spectroscopic view on cosmic PAH emission.” *Accounts of Chemical Research* 54 (2021): 1921–1933.

[17] Duley, W. “Chemical evolution of carbonaceous material in interstellar clouds.” *The Astrophysical Journal* 528 (2000): 841–848.

[18] Duley, W., S. Lazarev, and A. Scott. “Raman and infrared emission spectra of hydrogenated amorphous carbon: Insight into the origin of the 6-14 micron infrared emission bands.” *The Astrophysical Journal Letters* 620 (2005): L135–L138.

[19] Jones, A. “Variations on a theme–the evolution of hydrocarbon solids-i. Compositional and spectral modelling–the eRCN and DG models.” *Astronomy & Astrophysics* 540 (2012): A1–A12.

[20] Gadallah, K., H. Mutschke, and C. Jäger. “Mid-infrared spectroscopy of UV irradiated hydrogenated amorphous carbon materials.” *Astronomy & Astrophysics* 544 (2012): A107–A123.

[21] Papoular, R. “The use of kerogen data in understanding the properties and evolution of interstellar carbonaceous dust.” *Astronomy & Astrophysics* 378 (2001): 597–607.

[22] Cataldo, F., Y. Keheyan, and D. Heymann. “A new model for the interpretation of the unidentified infrared bands (UIBs) of the diffuse interstellar medium and of the protoplanetary nebulae.” *International Journal of Astrobiology* 1 (2002): 79–86.

[23] Kwok, S. and Y. Zhang. “Unidentified infrared emission bands: PAHs or MAONs?” *The Astrophysical Journal* 771 (2013): 5–23.

[24] Kwok, S. “Complex organics in space from solar system to distant galaxies.” *The Astronomy and Astrophysics Review* 24 (2016): 8–34.

[25] Sadjadi, S., S. Kwok, and Y. Zhang. “Theoretical infrared spectra of MAON molecules.” *Journal of Physics: Conference Series* 717 (2016): 062003.

[26] Cami, J., J. Bernard-Salas, E. Peeters, and S. E. Malek. “Detection of C_{60} and C_{70} in a young planetary nebula.” *Science* 329, no. 5996 (2010): 1180–1182.

[27] Bernard-Salas, J., J. Cami, E. Peeters, A. Jones, E. Micelotta, and M. Groenewegen. “On the excitation and formation of circumstellar fullerenes.” *The Astrophysical Journal* 757 (2012): 41.

[28] García-Hernández, D. A., E. Villaver, P. García-Lario, J. A. Acosta-Pulido, A. Manchado, L. Stanghellini, R. A. Shaw, and F. Cataldo. “Infrared study of fullerene planetary nebulae.” *The Astrophysical Journal* 760 (2012): 107.

[29] García-Hernández, D. A. “Dust and molecules in extra-galactic planetary nebulae.” *Proceedings of the International Astronomical Union* 11 (2015): E5.

[30] Otsuka, M., F. Kemper, J. Cami, E. Peeters, and J. Bernard-Salas. “Physical properties of fullerene-containing galactic planetary nebulae.” *Monthly Notices of the Royal Astronomical Society* 437 (2014): 2577–2593.

[31] Zhen, J., P. Castellanos, D. M. Paardekooper, H. Linnartz, and A. G. Tielens. “Laboratory formation of fullerenes from PAHs: Top-down interstellar chemistry.” *The Astrophysical Journal Letters* 797 (2014): L30.

[32] Chuvilin, A., U. Kaiser, E. Bichoutskaia, N. A. Besley, and A. N. Khlobystov. “Direct transformation of graphene to fullerene.” *Nature Chemistry* 2 (2010): 450–453.

[33] Hebgen, P., A. Goel, J. B. Howard, L. C. Rainey, and J. B. Vander Sande. "Synthesis of fullerenes and fullerenic nanostructures in a low-pressure benzene/oxygen diffusion flame." *Proceedings of the Combustion Institute* 28 (2000): 1397–1404.

[34] Baum, T., S. Löffler, P. Löffler, P. Weilmünster, and K.-H. Homann. "Fullerene ions and their relation to PAH and soot in low-pressure hydrocarbon flames." *Berichte der Bunsengesellschaft für Physikalische Chemie* 96 (1992): 841–857.

[35] Elvati, P., V. Dillstrom, and A. Violi. "Oxygen driven soot formation." *Proceedings of the Combustion Institute* 36 (2017): 825–832.

[36] Leon, G., W. J. Martin, E. J. Bringley, J. Akroyd, and M. Kraft. "The role of oxygenated species in the growth of graphene, fullerenes and carbonaceous particles." *Carbon* 182 (2021): 203–213.

[37] Carpentier, Y., G. Féraud, E. Dartois, R. Brunetto, E. Charon, A.-T. Cao, L. d'Hendecourt, P. Bréchignac, J.-N. Rouzaud, and T. Pino. "Nanostructuration of carbonaceous dust as seen through the positions of the 6.2 and 7.7 μm AIBs." *Astronomy & Astrophysics* 548 (2012): A40.

[38] Pino, T., E. Dartois, A.-T. Cao, Y. Carpentier, T. Chamaillé, R. Vasquez, A. Jones, L. d'Hendecourt, and P. Bréchignac. "The 6.2 band position in laboratory and astrophysical spectra: A tracer of the aliphatic to aromatic evolution of interstellar carbonaceous dust." *Astronomy & Astrophysics* 490 (2008): 665–672.

[39] Spilker, J. S., K. A. Phadke, M. Aravena, M. Archipley, M. B. Bayliss, J. E. Birkin, M. Béthermin, J. Burgoyne, J. Cathey, S. C. Chapman *et al.* "Spatial variations in aromatic hydrocarbon emission in a dust-rich galaxy." *Nature* 618 (2023): 708–711.

[40] Lyu, J., X. Yang, A. Li, F. Sun, G. H. Rieke, S. Alberts, and I. Shivaei. "Unveiling the aromatic and aliphatic universe at redshifts $z \sim 0.2$–0.5 with JWST NIRCam/WFSS." *The Astrophysical Journal* 986 (2025): 156.

[41] Young, J., A. Pope, A. Sajina, L. Yan, T. S. Goncalves, M. Eleazer, S. Alberts, L. Armus, M. Bonato, D. A. Dale *et al.* "Halfway to the peak: Spatially resolved star formation and kinematics in a $z = 0.54$ dusty galaxy with JWST/MIRI." *The Astrophysical Journal Letters* 958 (2026): L5.

[42] Sajina, A., A. Pope, H. Spoon, L. Armus, M. Eleazer, D. Farrah, M. Lacy, T. Lai, J. McKinney, S. Veilleux *et al.* "Halfway to the peak: Ice absorption bands at $z \approx 0.5$ with JWST MIRI/MRS." *The Astrophysical Journal* 985 (2025): 201.

[43] Mattioda, A., C. Bauschlicher, Jr., A. Ricca, J. Bregman, D. Hudgins, and L. Allamandola. "Infrared spectroscopy of matrix-isolated neutral polycyclic aromatic nitrogen heterocycles: The acridine series." *Spectrochimica Acta Part A: Molecular and Biomolecular Spectroscopy* 181 (2017): 286–308.

[44] Ricca, A., C. W. Bauschlicher, Jr., C. Boersma, A. G. Tielens, and L. J. Allamandola. "The infrared spectroscopy of compact polycyclic aromatic hydrocarbons containing up to 384 carbons." *The Astrophysical Journal* 754 (2012): 75.

[45] Maltseva, E., A. Petrignani, A. Candian, C. J. Mackie, X. Huang, T. J. Lee, A. G. Tielens, J. Oomens, and W. J. Buma. "High-resolution IR absorption spectroscopy of polycyclic aromatic hydrocarbons in the 3 μm region: Role of periphery." *The Astrophysical Journal* 831 (2016): 58.

[46] Candian, A., P. Sarre, and A. Tielens. "Polycyclic aromatic hydrocarbons with armchair edges and the 12.7 μm band." *The Astrophysical Journal Letters* 791 (2014): L10.

[47] Ricca, A., J. E. Roser, C. Boersma, E. Peeters, and A. Maragkoudakis. "Role of Polycyclic Aromatic Hydrocarbons with Edge Defects in Explaining Astronomical Infrared Emission Observations." 968, no. 2 (2024): 128.

[48] Peeters, E., E. Habart, O. Berné, A. Sidhu, R. Chown, D. Van De Putte, B. Trahin, I. Schroetter, A. Canin, F. Alarcón *et al.* "Pdrs4all-iii. jwst's nir spectroscopic view of the orion bar." *Astronomy & Astrophysics* 685 (2024): A74.

[49] Kirkpatrick, A., A. Pope, A. Sajina, E. Roebuck, L. Yan, L. Armus, T. Díaz-Santos, and S. Stierwalt. "The role of star formation and an agn in dust heating of z= 0.3–2.8 galaxies. i. evolution with redshift and luminosity." *The Astrophysical Journal* 814, no. 1 (2015): 9.

[50] Inami, H., L. Armus, H. Matsuhara, V. Charmandaris, T. Díaz-Santos, J. Surace, S. Stierwalt, Y. Ohyama, J. Howell, J. Marshall *et al.* "The AKARI 2.5–5 micron spectra of luminous infrared galaxies in the local universe." *Astronomy & Astrophysics* 617 (2018): A130.

[51] Lebouteiller, V., D. Barry, H. Spoon, J. Bernard-Salas, G. Sloan, J. Houck, and D. Weedman. "CASSIS: The Cornell atlas of spitzer/infrared spectrograph sources." *The Astrophysical Journal Supplement Series* 196 (2011): 8.

[52] García-Bernete, I., D. Rigopoulou, A. Alonso-Herrero, M. Pereira-Santaella, P. Roche, and B. Kerkeni. "Polycyclic aromatic hydrocarbons in seyfert and star-forming galaxies." *Monthly Notices of the Royal Astronomical Society* 509 (2022): 4256–4275.

[53] Hrodmarsson, H. R., I. Aleman, A. Candian, S. Wiersma, J. Palotás, D. Dubois, A. Sidhu, D. Loru, P. Sundararajan, E. Sciamma-O'Brien *et al.* "The AstroPAH 10 years of science review." *Space Science Reviews* 221 (2025): 42.

[54] Esquej, P., A. Alonso-Herrero, O. González-Martín, S. F. Hönig, A. Hernán-Caballero, P. Roche, C. Ramos Almeida, R. E. Mason, T. Díaz-Santos, N. A. Levenson *et al.* "Nuclear star formation activity and black hole accretion in nearby seyfert galaxies." *The Astrophysical Journal* 780 (2014): 86.

[55] Zang, R. X., E. Maragkoudakis, and E. Peeters. "The spatially resolved PAH characteristics in the whirlpool galaxy (M51a)." *Monthly Notices of the Royal Astronomical Society* 511 (2022): 5142–5157.

[56] García-Bernete, I., C. Ramos Almeida, H. Landt, M. Ward, M. Baloković, and J. Acosta-Pulido. "The infrared to x-ray correlation spectra of unobscured type 1 active galactic nuclei." *Monthly Notices of the Royal Astronomical Society* 469 (2017): 110–126.

[57] Kewley, L. J., B. Groves, G. Kauffmann, and T. Heckman. "The host galaxies and classification of active galactic nuclei." *Monthly Notices of the Royal Astronomical Society* 372 (2006): 961–976.

[58] Roser, J., A. Ricca, and L. Allamandola. "Anthracene clusters and the interstellar infrared emission features." *The Astrophysical Journal* 783 (2014): 97.

[59] Roser, J. and A. Ricca. "Polycyclic aromatic hydrocarbon clusters as sources of interstellar infrared emission." *The Astrophysical Journal* 801 (2015): 108.

[60] Rap, D. B., J. G. Schrauwen, A. N. Marimuthu, B. Redlich, and S. Brünken. "Low-temperature nitrogen-bearing polycyclic aromatic hydrocarbon formation routes validated by infrared spectroscopy." *Nature Astronomy* 6 (2022): 1059–1067.

[61] Palotás, J., J. Martens, G. Berden, and J. Oomens. "The infrared spectrum of protonated C_{70}." *The Astrophysical Journal Letters* 909 (2021): L17.

[62] McGuire, B. A. "2021 census of interstellar, circumstellar, extragalactic, protoplanetary disk, and exoplanetary molecules." *The Astrophysical Journal Supplement Series* 259 (2022): 30.

[63] Hou, G.-L., O. V. Lushchikova, J. M. Bakker, P. Lievens, L. Decin, and E. Janssens. "Buckyball-metal complexes as potential carriers of astronomical unidentified infrared emission bands." *The Astrophysical Journal* 952 (2023): 13.

[64] Campbell, E. K., M. Holz, D. Gerlich, and J. P. Maier. "Laboratory confirmation of C_{60}^+ as the carrier of two diffuse interstellar bands." *Nature* 523 (2015): 322–323.

[65] Bull, J. N., J. T. Buntine, M. S. Scholz, E. Carrascosa, L. Giacomozzi, M. H. Stockett, and E. J. Bieske. "Photodetachment and photoreactions of substituted naphthalene anions in a tandem ion mobility spectrometer." *Faraday Discussions* 217 (2019): 34–46.

[66] Lee, J. W., M. H. Stockett, E. K. Ashworth, J. E. Navarro Navarrete, E. Gougoula, D. Garg, M. Ji, B. Zhu, S. Indrajith, H. Zettergren *et al.* "Cooling dynamics of energized naphthalene and azulene radical cations." *The Journal of Chemical Physics* 158, no. 15 (2023): 154304.

[67] Schmidt, H. T., R. D. Thomas, M. Gatchell, S. Rosén, P. Reinhed, P. Löfgren, L. Brännholm, M. Blom, M. Björkhage, E. Bäckström *et al.* "First storage of ion beams in the double electrostatic ion-ring experiment: DESIREE." *Review of Scientific Instruments* 84, no. 5 (2013): 055115.

[68] Stockett, M. H., J. N. Bull, H. Cederquist, S. Indrajith, M. Ji, J. E. Navarro Navarrete, H. T. Schmidt, H. Zettergren, and B. Zhu. "Efficient stabilization of cyanonaphthalene by fast radiative cooling and implications for the resilience of small PAHs in interstellar clouds." *Nature Communications* 14 (2023): 395.

[69] Contreras, C. S. and F. Salama. "Laboratory Investigations of Polycyclic Aromatic Hydrocarbon Formation and Destruction in the Circumstellar Outflows of Carbon Stars." 208, no. 1 (2013): 6.

[70] Muñoz Caro, G. M., H. Carrascosa de Lucas, and R. Martín-Doménech. "Photochemistry of interstellar ice forming complex organic molecules." *Nature Reviews Chemistry* 9 (2025): 537–552.

[71] Escribano, R. and G. M. Muñoz Caro. "Introduction to spectroscopy and astronomical observations."*In* , 27–47. Springer, 2018.

[72] Schneider, H., A. Caldwell-Overdier, S. Coppieters 't Wallant, L. Dau, J. Huang, I. Nwolah, M. Kasule, C. Buffo, E. Mullikin, L. Widdup *et al.* "Detection of methoxymethanol as a photochemistry product of condensed methanol." *Monthly Notices of the Royal Astronomical Society: Letters* 485 (2019): L19–L23.

[73] Öberg, K. I., R. T. Garrod, E. F. van Dishoeck, and H. Linnartz. "Formation rates of complex organics in UV irradiated CH_3OH-rich ices-i. Experiments." *Astronomy & Astrophysics* 504 (2009): 891–913.

[74] Muñoz Caro, G., U. J. Meierhenrich, W. A. Schutte, B. Barbier, A. Arcones Segovia, H. Rosenbauer, W.-P. Thiemann, A. Brack, and J. M. Greenberg. "Amino acids from ultraviolet irradiation of interstellar ice analogues." *Nature*

416 (2002): 403–406.

[75] Bernstein, M. P., J. P. Dworkin, S. A. Sandford, G. W. Cooper, and L. J. Allamandola. "Racemic amino acids from the ultraviolet photolysis of interstellar ice analogues." *Nature* 416 (2002): 401–403.

[76] Fortenberry, R. C. "Quantum astrochemical spectroscopy." *International Journal of Quantum Chemistry* 117 (2017): 81–91.

[77] Zapata Trujillo, J. C., M. M. Pettyjohn, and L. K. McKemmish. "High-throughput quantum chemistry: Empowering the search for molecular candidates behind unknown spectral signatures in exoplanetary atmospheres." *Monthly Notices of the Royal Astronomical Society* 525 (2023): 361–376.

[78] Mackie, C. J., A. Candian, X. Huang, E. Maltseva, A. Petrignani, J. Oomens, W. J. Buma, T. J. Lee, and A. G. Tielens. "The anharmonic quartic force field infrared spectra of hydrogenated and methylated PAHs." *Physical Chemistry Chemical Physics* 20 (2018): 1189–1197.

[79] Mackie, C. J., T. Chen, A. Candian, T. J. Lee, and A. G. Tielens. "Fully anharmonic infrared cascade spectra of polycyclic aromatic hydrocarbons." *The Journal of Chemical Physics* 149, no. 4 (2018): 044307.

[80] Kerkeni, B., M. Boukallaba, M. Hechmi, D. Duflot, and C. Toubin. "QM/MM study of the H_2 formation on the surface of a water ice grain doped with formaldehyde: Molecular dynamics and reaction kinetics." *Frontiers in Astronomy and Space Sciences* 9 (2022): 807649.

[81] Vydrov, O. A. and T. Van Voorhis. "Benchmark assessment of the accuracy of several van der Waals density functionals." *Journal of Chemical Theory and Computation* 8 (2012): 1929–1934.

[82] Sadjadi, S., Q. A. Parker, C.-H. Hsia, and Y. Zhang. "A theoretical study of infrared spectra of highly positively charged C_{60} fullerenes and their relevance to observed UIE features." *The Astrophysical Journal* 934 (2022): 75.

[83] Lee, K. L. K., J. Patterson, A. M. Burkhardt, V. Vankayalapati, M. C. McCarthy, and B. A. McGuire. "Machine learning of interstellar chemical inventories." *The Astrophysical Journal Letters* 917 (2021): L6.

[84] Fried, Z. T., K. L. K. Lee, A. N. Byrne, and B. A. McGuire. "Implementation of rare isotopologues into machine learning of the chemical inventory of the solar-type protostellar source IRAS 16293-2422." *Digital Discovery* 2 (2023): 952–966.

[85] Marks, N. "Thin film deposition of tetrahedral amorphous carbon: A molecular dynamics study." *Diamond and Related Materials* 14 (2005): 1223–1231.

[86] Behler, J. and M. Parrinello. "Generalized neural-network representation of high-dimensional potential-energy surfaces." *Physical Review Letters* 98 (2007): 146401.

[87] Zarrouk, T., R. Ibragimova, A. P. Bartók, and M. A. Caro. "Experiment-driven atomistic materials modeling: A case study combining x-ray photoelectron spectroscopy and machine learning potentials to infer the structure of oxygen-rich amorphous carbon." *Journal of the American Chemical Society* 146 (2024): 14 645–14 659.

[88] Austin, S., P. Fowler, P. Hansen, D. Monolopoulos, and M. Zheng. "Fullerene isomers of C_{60}. Kekulé counts versus stability." *Chemical Physics Letters* 228 (1994): 478–484.

[89] Frenklach, M. and E. D. Feigelson. "Formation of polycyclic aromatic hydrocarbons in circumstellar envelopes." *The Astrophysical Journal* 341 (1989): 372–384.

[90] Cole, J., J. Bittner, J. Longwell, and J. Howard. "Formation mechanisms of aromatic compounds in aliphatic flames." *Combustion and Flame* 56 (1984): 51–70.

[91] Massa, D., K. D. Gordon, and E. Fitzpatrick. "Relations between mid-infrared dust emission and UV extinction." *The Astrophysical Journal* 925 (2022): 19.

[92] Díaz-Luis, J., D. García-Hernández, A. Manchado, P. García-Lario, E. Villaver, and G. García-Segura. "GTC/CanariCam mid-IR imaging of the fullerene-rich planetary nebula IC 418: Searching for the spatial distribution of fullerene-like molecules." *The Astronomical Journal* 155 (2018): 105.

[93] Fan, H., L. Hobbs, J. A. Dahlstrom, D. E. Welty, D. G. York, B. Rachford, T. P. Snow, P. Sonnentrucker, N. Baskes, and G. Zhao. "The Apache Point Observatory catalog of optical diffuse interstellar bands." *The Astrophysical Journal* 878 (2019): 151.

[94] Cox, N., J. Cami, L. Laper, P. Ehrenfreund, B. Foing, B. Ochsendorf, S. Van Hooff, and F. Salama. "VLT/X-shooter survey of near-infrared diffuse interstellar bands." *Astronomy & Astrophysics* 569 (2014): A117.

[95] Elyajouri, M., R. Lallement, N. Cox, J. Cami, M. Cordiner, J. Smoker, A. Fahrang, P. Sarre, and H. Linnartz. "The EDIBLES survey-III. C_2-DIBs and their profiles." *Astronomy & Astrophysics* 616 (2018): A143.

[96] Rasmussen, A. P., G. Wenzel, L. Hornekær, and L. H. Andersen. "Gas-phase electronic action absorption spectra of protonated oxygen-functionalized polycyclic aromatic hydrocarbons (OPAHs)." *Astronomy & Astrophysics* 674

(2023): A103.

[97] Murga, M. S. “Evolution of carbon particles from the stage of asymptotic giant branch stars to planetary nebulae: Observations, experiments, and theory.” *Uspekhi Fizicheskikh Nauk* 194 (2024): 1017–1045.

[98] Alonso-Herrero, A., C. Ramos Almeida, P. Esquej, P. Roche, A. Hernán-Caballero, S. Hönig, O. González-Martín, I. Iretxaga, R. Mason, C. Packham *et al.* “Nuclear 11.3 μm PAH emission in local active galactic nuclei.” *Monthly Notices of the Royal Astronomical Society* 443 (2014): 2766–2782.

Information about authors

Aliya Tychengulova *– Postdoctoral Researcher at Abai Kazakh National Pedagogical University, Physics Department, Almaty, Kazakhstan, e-mail: : a.tychengulova@gmail.com.*

IRSTI 30.51.31 https://doi.org/10.51889/IJAPA.2026.1.1.003

CONVECTIVE INSTABILITY TRIGGERED BY A DILUTE SOLID PHASE IN THE $CO_2 - Si - N_2$ GAS–AEROSOL SYSTEM AT LOW PARTICLE LOADING: A NUMERICAL STUDY

V. Mukamedenkyzy[1] **and A. Tolepbergen**[1*]

[1] *Al-Farabi Kazakh National University, Almaty, Kazakhstan*

*Corresponding Author: arsen4236@gmail.com

Received 18 May 2026; Accepted 4 June 2026

Abstract. This paper reports a numerical investigation of diffusion-convective mass transfer in the $CO_2 - Si - N_2$ gas–aerosol system at a low dispersed-phase volume fraction of $\phi = 0.5\%$ under isothermal and isobaric conditions($T = 300$ K, $p = 0.1$ MPa). Computations were carried out in ANSYS Fluent, combining the Species Transport formulation with the Eulerian Multiphase Flow framework, which together capture the coupled motion of gas components and solid microparticles with a diameter of 10 μm. The results demonstrate that even at such a low particle loading, gravitational settling of *Si* particles generates a local density inversion near the bottom wall of the upper vessel – sufficient to trigger convective instability. The mixing evolves through a sequence of well-defined stages: initial particle sedimentation, formation and subsequent breakup of a dense particle cluster, sustained downward transport through the connecting channel, and the emergence of a characteristic teardrop-shaped solid-phase structure in the lower vessel. Throughout this process, the two phases exhibit markedly different transport kinetics: CO_2 accumulates gradually and continuously, whereas Si migrates in discrete pulses, producing pronounced oscillations in the dispersed-phase volume fraction. The principal novelty of this work lies in demonstrating that Rayleigh–Taylor-type convective instability develops at $\phi = 0.5\%$ – a loading level at which any solid-phase influence on the mass transfer mechanism would not be expected a priori. This finding points to the existence of a lower concentration threshold below which the system transitions from gas–like diffusive behavior to a qualitatively different convection-driven regime. The combined Species Transport and Eulerian Multiphase approach proves capable of reproducing diffusion – convective dynamics in dilute gas–solid systems without recourse to empirical fitting parameters. The outcomes of this study are relevant to modeling aerosol particle behavior under atmospheric and industrial conditions, and may inform the design of experiments aimed at measuring mutual diffusion coefficients in gas–aerosol systems.

Keywords: gas–aerosol system, diffusion-convective mass transfer, Rayleigh–Taylor instability, dispersed phase, silicon, ANSYS Fluent, Eulerian multiphase approach, concentration-driven convection, gravitational sedimentation, Species Transport.

1. INTRODUCTION

Diffusion-convective mass transfer in gas–solid systems underpins a broad range of natural and industrial phenomena, spanning atmospheric aerosol transport, particulate emissions from combustion facilities, and mixing in chemical reactors. Many practically relevant configurations of this kind operate under isothermal and isobaric conditions, yet their dynamics remain poorly understood owing to the intricate interplay between molecular diffusion, concentration-driven gravitational convection, and inertial settling of the dispersed phase.

In isothermal multicomponent gas mixtures, a pronounced mismatch in component diffusivities can destabilize the mechanical equilibrium of the system [1, 2]. Depending on the balance between partial concentration gradients and the thermophysical properties of the mixture, regions of locally elevated or reduced density may arise [3, 4, 5], driving concentration-induced gravitational convection.

The threshold conditions for this instability admit determination by experimental means [6], through analytical treatment within Rayleigh stability theory [1, 6], or via numerical simulation [7, 8]. A systematic review of the phenomenon in gas mixtures is available in [9].

Earlier work [1, 9] addressed primarily configurations in which mixture density decreases with height – a stratification that suppresses convective perturbations. The present study turns to the opposite arrangement: an upward-directed density gradient, which gives rise to Rayleigh–Taylor convection [10]. In gas–solid systems, this instability takes on a distinctive character – the solid dispersed phase locally elevates the mixture density in the upper region, establishing a density inversion that drives the formation of descending particle jets and convective cells. While Rayleigh–Taylor dynamics have been thoroughly examined in gas–liquid and gas–gas configurations [10, 11, 12], analogous behavior in dilute gas–solid systems – where particle loading is low enough that the very onset of instability remains an open question – has received considerably less scrutiny.

A central unresolved question concerns the minimum solid-phase volume fraction ϕ at which the dispersed component begins to appreciably alter the mass transfer mechanism. In the limiting case of $\phi \to 0$, the system reduces to a binary gas mixture governed entirely by molecular diffusion. As ϕ increases, the solid phase contributes to local density stratification and interphase momentum exchange, ultimately giving rise to convective structures.

Experimental access to such processes is hindered by the optical opacity of particle-laden media, micro-scale interfacial effects, and the inherently transient nature of the phase boundary [13, 14, 15, 16]. Computational fluid dynamics offers a practical alternative, providing spatially and temporally resolved descriptions of multicomponent multiphase flows. Nevertheless, most available numerical models are tailored either to dense suspensions or rely on empirical closure terms that restrict their validity in dilute flow regimes [17, 18, 19, 20, 21].

The present work addresses this gap through a detailed CFD study of diffusion-convective mixing in the $CO_2 - Si - N_2$ gas–aerosol system at an initial solid-phase volume fraction of $\phi = 0.5\%$. The numerical framework couples the Species Transport equations – previously validated for ternary gas systems [22, 23] – with the Eulerian Multiphase Flow method, which accounts for interphase momentum exchange without invoking empirical corrections. The core objective is to establish whether such a low particle loading is capable of qualitatively altering the mass transfer regime relative to a pure gas system, and if so, to identify the governing mechanisms and the characteristic timescales of each process stage. The critical loading ϕ_{cr} marking this transition has not been systematically characterized for gas–solid systems under isothermal and isobaric conditions, and closing this gap constitutes the primary motivation of the present study.

2. METHODOLOGY

The system under study comprises two cylindrical vessels arranged vertically and connected by a narrow cylindrical channel. At the initial moment, the upper vessel contains a mixture of CO_2 gas and solid Si microparticles at a prescribed volume fraction ϕ, while the lower vessel holds pure N_2. All calculations were performed under isothermal and isobaric conditions at $T = 300$ K and $p = 0.1$ MPa. The computational domain geometry (Figure 1) reproduces the configuration employed in earlier work [22, 23]: each vessel measures 47.5 mm in height, the connecting channel is 70 mm tall with an inner diameter of 6.1 mm. All walls are treated as impermeable, adiabatic, and no-slip.

The thermophysical properties of the gas components and solid particles are listed in Table 1. The density and viscosity values of each constituent directly govern the nature of interphase interactions and the intensity of convective structures that develop during mixing. Of particular significance is the substantial density contrast between the gas phase (CO_2, N_2) and the solid Si particles

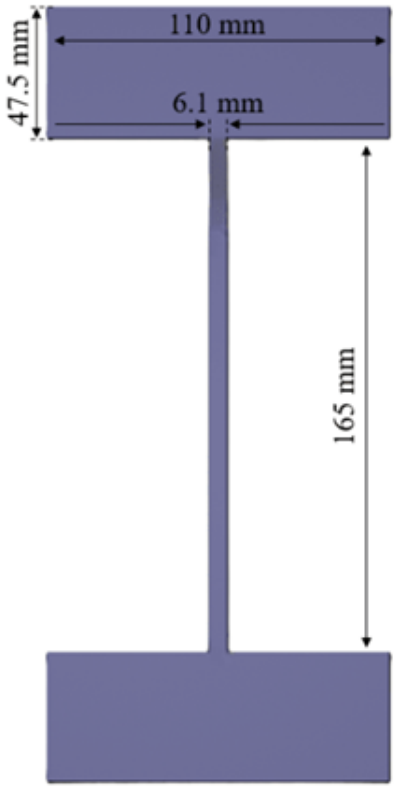

Figure 1 – Geometric model of the study area.

($\rho = 2330$ kg/m^3), which amplifies the gravitational contribution to dispersed-phase dynamics and constitutes the primary factor controlling the conditions under which density inversion occurs.

Table 1. Thermophysical properties of gases and particles.

Component	**Phase type**	**Molar mass**, g/mol	**Density**, kg/m^3	**Viscosity**, Pa·s	**Thermal cond.**, W/(m·K)	c_p, J/(kg·K)
CO_2	gas	44.01	1.977	1.48×10^{-5}	0.0166	844
Si	solid	28.09	2330	—	148.0	700
N_2	gas	28.02	1.165	1.76×10^{-5}	0.0259	1040

The computational approach builds on a gas diffusion model validated in prior work [22, 23], extended here to incorporate a solid dispersed phase. Gas-phase species transport is handled through the Species Transport equations under isothermal and isobaric conditions, with turbulence closure provided by the SST $k-\omega$ model. The solid phase is treated within the Eulerian Multiphase Flow framework, in which both the gas and solid constituents are modelled as interpenetrating continua, each carrying its own velocity, pressure, and volume fraction fields. Mass conservation for phase q is expressed through the continuity equation:

$$\frac{\partial}{\partial t}(\alpha_q \rho_q) + \nabla \cdot (\alpha_q \rho_q \vec{v}_q) = \sum_{p=1}^{n} (\dot{m}_{pq} - \dot{m}_{qp}) + S_q \tag{1}$$

where the source terms represent the phase transition rate and characterise mass exchange between phases p and q in both directions [24]. Since no phase transitions or chemical reactions occur in this

configuration, these terms vanish identically.

The momentum balance for phase q takes the form:

$$\begin{aligned}\frac{\partial}{\partial t}(\alpha_q\rho_q\vec{v}_q)+\nabla\cdot(\alpha_q\rho_q\vec{v}_q\vec{v}_q) = &-\alpha_q\nabla p+\nabla\cdot\vec{\tau}_q+\alpha_q\rho_q\vec{g}\\ &+\sum_{p=1}^{n}(\vec{R}_{pq}+\dot{m}_{pq}\vec{v}_{pq}-\dot{m}_{qp}\vec{v}_{qp})\\ &+(\vec{F}_q+\vec{F}_{\text{lift},q}+\vec{F}_{\text{wl},q}+\vec{F}_{\text{vm},q}+\vec{F}_{\text{ud},q})\end{aligned} \tag{2}$$

where the stress-strain tensor, effective phase density, and body-force contributions are defined in accordance with the standard Eulerian multiphase formulation [24]. The gravitational term plays a central role in this problem: the density inversion between the particle-laden upper region and the pure gas in the lower vessel acts as the driving force behind Rayleigh–Taylor-type instability.

Interphase momentum exchange between the gas and solid phases is given by:

$$\sum_{p=1}^{n}\vec{R}_{pq}=\sum_{p=1}^{n}K_{pq}(\vec{v}_p-\vec{v}_q) \tag{3}$$

where K_{pq} is the interphase momentum transfer coefficient, evaluated from the Schiller–Naumann drag correlation for spherical particles of diameter $d_p = 10^{-5}$ m.

The volume fraction of each phase is obtained by solving the transport equation:

$$\frac{1}{\rho_{rq}}\left(\frac{\partial}{\partial t}(\alpha_q\rho_q)+\nabla\cdot(\alpha_q\rho_q\vec{v}_q)\right)=\sum_{p=1}^{n}(\dot{m}_{pq}-\dot{m}_{qp}) \tag{4}$$

subject to the constraint that all phase volume fractions sum to unity.

The momentum balance for the solid phase s, accounting for particle pressure and granular stresses, reads:

$$\begin{aligned}\frac{\partial}{\partial t}(\alpha_s\rho_s\vec{v}_s)+\nabla\cdot(\alpha_s\rho_s\vec{v}_s\vec{v}_s) = &-\alpha_s\nabla p-\nabla p_s+\nabla\cdot\vec{\tau}_s+\alpha_s\rho_s\vec{g}\\ &+\sum_{l=1}^{N}(K_{ls}(\vec{v}_l-\vec{v}_s)+\dot{m}_{ls}\vec{v}_{ls}-\dot{m}_{sl}\vec{vxl}_{sl})\\ &+(\vec{F}_s+\vec{F}_{\text{lift},s}+\vec{F}_{\text{wl},s}+\vec{F}_{\text{vm},s}+\vec{F}_{\text{td},s})\end{aligned} \tag{5}$$

The rheological behaviour of the solid phase is described within the kinetic theory of granular flows. By analogy with molecular motion in a gas, the random translational velocity of particles arising from inter-particle collisions is characterised by a granular temperature Θ_s defined as one third of the mean square of the particle velocity fluctuation. This quantity governs the effective pressure, viscosity, and normal stresses of the solid phase, and accounts for the partially inelastic nature of collisions. The granular temperature is solved as an additional transport equation coupled to the solid-phase momentum balance (Equation (5)).

The initial conditions are as follows: upper vessel – a mixture of CO_2 and solid Si particles at a volume fraction of $\phi = 0.5\%$; lower vessel and channel – pure N_2 ($\phi = 0$).

No-slip conditions are imposed on all walls for the gas phase, and a particle adhesion condition is applied for the solid phase. Pressure and temperature are held constant throughout the domain at $p = 0.1$ MPa and $T = 300$ K.

All simulations were carried out in a transient formulation with a time step of 1 s over 1200 steps, covering 20 minutes of physical process time. A pressure-based coupled solver was employed,

providing full pressure-velocity coupling within each iteration. Convective terms were discretised using the Second Order Upwind scheme, while pressure interpolation relied on the PRESTO! scheme, which delivers improved accuracy in the presence of body forces. Time integration was performed with a second-order implicit scheme.

The computational mesh had a structured topology comprising 164 120 cells and 165 974 nodes. The minimum cell size in the channel region was set to 0.25 mm, ensuring adequate resolution of local concentration and velocity gradients at the interphase boundaries. Convergence criteria were set to 10^{-6} for the velocity and pressure fields and 10^{-8} for species concentrations and phase volume fractions.

3. Results and Discussion

Mixing in the $CO_2 - Si - N_2$ system at $\phi = 0.5\%$ is strongly non-stationary and unfolds through a succession of distinct stages that set the gas–aerosol system apart from purely gaseous mixing. Each stage is examined below on the basis of spatial distributions of the dispersed phase and temporal concentration profiles of the individual components.

Immediately after the partition is opened, Si particles initially distributed uniformly throughout the upper vessel begin to settle under gravity. By $t \approx 40 - 50$ s, virtually the entire dispersed phase has accumulated into a thin layer along the bottom wall of the upper vessel. During this interval, CO_2 starts to penetrate the lower vessel through the connecting channel, though the transfer rate remains low and consistent with a diffusion-controlled regime. The temporal profile of the CO_2 mole fraction in the lower vessel (Figure3 a) shows a slow, monotonic rise from zero to values on the order of $0.002 - 0.003$, characteristic of purely diffusive transport. The Si volume fraction in the lower vessel (Figure3 b) stays essentially at zero throughout this period, as no particles have yet reached the channel entrance. At this stage, therefore, the two phases evolve largely independently of one another – the gas diffuses while the solid sediments.

As particles accumulate along the bottom wall of the upper vessel, the local mixture density in that zone rises sharply, establishing a density inversion in which a heavier layer sits above the comparatively light gas in the lower vessel. This configuration satisfies the classical conditions for Rayleigh–Taylor instability. Around $t \approx 100 - 105$ s, a characteristic disturbance develops in the upper vessel: the dense particle cluster that has built up near the bottom wall lifts upward and subsequently breaks apart into numerous smaller fragments. On the CO_2 mole fraction profile (Figure3 a), the transition to convective transport manifests as a pronounced increase in the slope of the curve near $t \approx 100 - 105$ s. The Si volume fraction trace (Figure3 b) shows a sharp upward spike at the same moment, reflecting the impulsive entrainment of dispersed-phase fragments into convective motion. This juncture marks the crossover from diffusion-dominated to convection-dominated behaviour – a transition that occurs at $\phi = 0.5\%$ — a loading level at which any solid-phase influence would not be anticipated a priori, and which constitutes one of the principal findings of this study.

Following cluster breakup, the dispersed-phase fragments are swept into the downward convective current and begin entering the connecting channel. By $t \approx 220 - 270$ s, particle flow through the channel has reached a quasi-steady character. At this point, the CO_2 mole fraction in the lower vessel (Figure3 a) has climbed to values in the range $0.08 - 0.10$ – several times higher than would be expected from purely diffusive transport over the same time interval. The Si volume fraction (Figure3 b) over this period exhibits a series of decaying oscillations with an amplitude of approximately $0.002 - 0.003$, each peak corresponding to a discrete pulse of particles arriving through the channel. The contrast in phase kinetics at this stage is fundamental: CO_2 accumulates smoothly and continuously, whereas Si arrives in intermittent bursts tied to individual convective events.

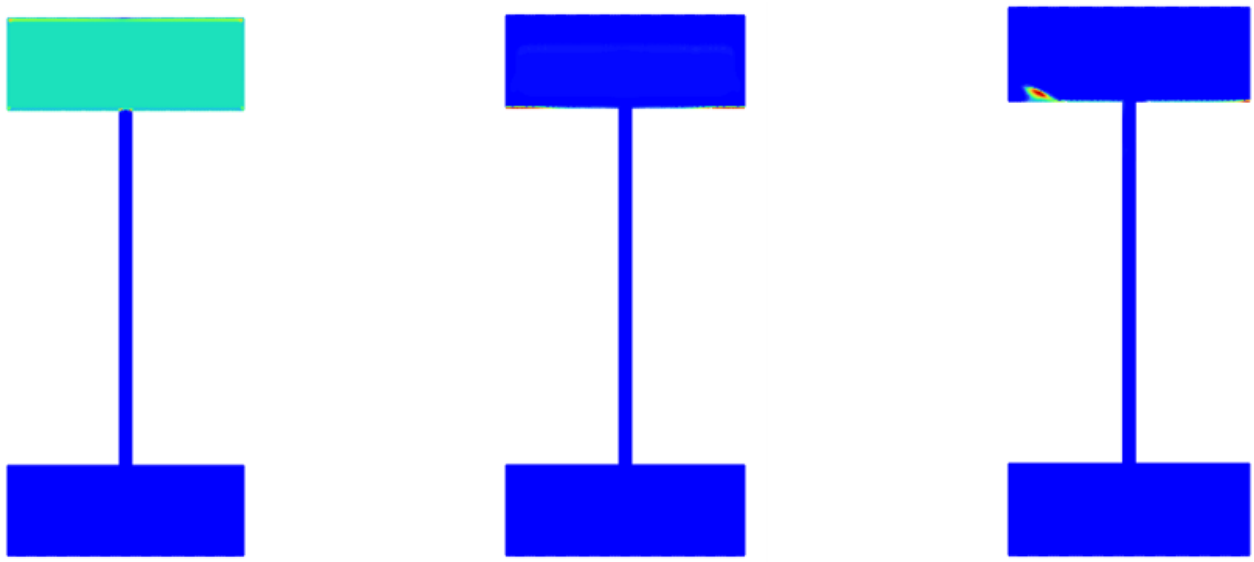

(a) $t = 0$ s **(b)** $t = 50$ s **(c)** $t = 105$ s

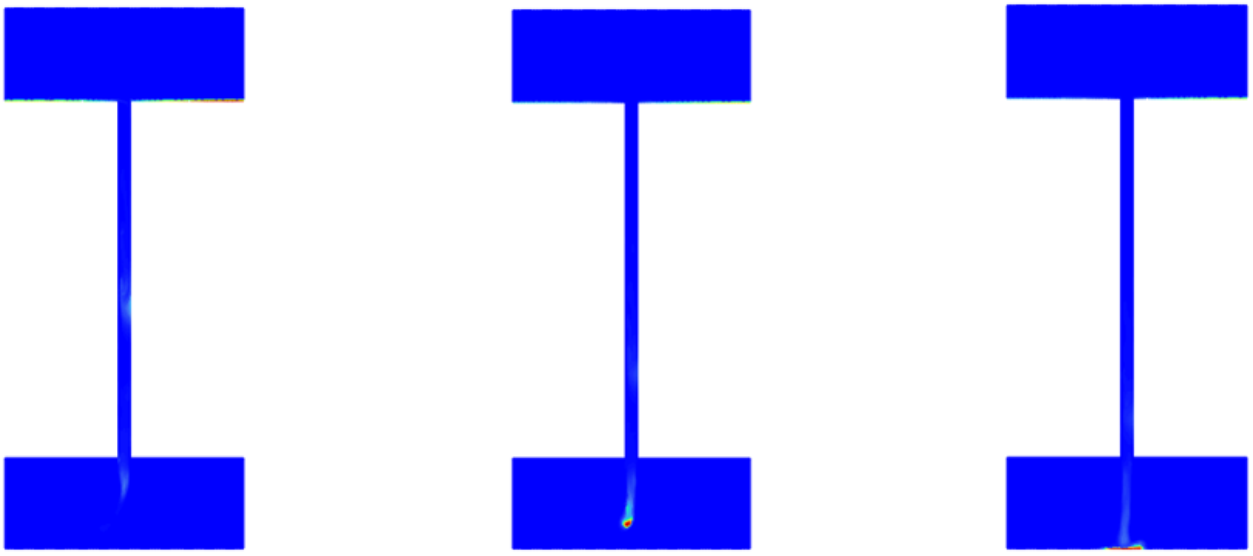

(d) $t = 255$ s **(e)** $t = 280$ s **(f)** $t = 300$ s

Figure 2 – Spatial distribution of the Si particle volume fraction in the $CO_2 + 0.005\,Si - N_2$ system at $p = 0.1$ MPa, $T = 300$ K at successive time instants: a) $t = 0$ s – uniform distribution of the dispersed phase throughout the upper vessel; b) $t = 50$ s – particle sedimentation onto the bottom wall of the upper vessel; c) $t = 105$ s — onset of convective disturbance and breakup of the dispersed-phase cluster; d) $t = 255$ s – downward particle flow through the connecting channel; e) $t = 280$ s – formation of a teardrop-shaped dispersed-phase structure in the lower vessel; f) $t = 300$ s – final distribution of particles along the bottom of the lower vessel.

Upon reaching the lower vessel, the particle stream consolidates into a compact teardrop-shaped structure of elevated local dispersed-phase concentration. Clearly resolved at $t \approx 280$ s (Figure 2c), this morphology represents a direct signature of Rayleigh–Taylor instability in a gas–solid medium – the solid-phase analogue of the density fingers characteristic of classical RT convection. By $t \approx 300$ s, the structure settles onto the floor of the lower vessel and spreads gradually across its surface. Beyond $t = 300$ s, both concentration profiles enter a quasi-stationary regime: the CO_2 curve (Figure 3 a)

continues to rise slowly, approaching an asymptotic value of approximately $0.10 - 0.11$, while the Si trace (Figure3 b) levels off at around $0.004 - 0.005$, reflecting near-complete displacement of the dispersed phase into the lower vessel.

Taken together, these observations confirm that at $\phi = 0.5\%$ the presence of the solid dispersed phase qualitatively reshapes the mass transfer mechanism relative to a pure gas system. Particle accumulation at the bottom of the upper vessel generates sufficient local density stratification to exceed the threshold for convective instability. The two phases respond to this instability in fundamentally different ways: the gas phase undergoes a gradual, continuous acceleration in transport, whereas the solid phase migrates through a sequence of discrete impulsive events, each linked to an individual convective episode. This divergence reflects a deep asymmetry in the inertial properties of the two phases and in the way each interacts with the gravitational field.

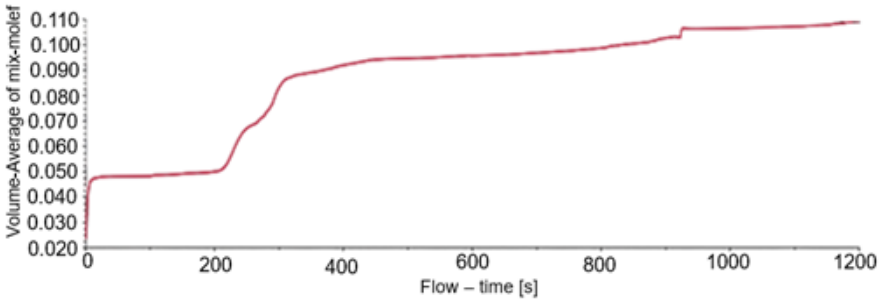

(a)

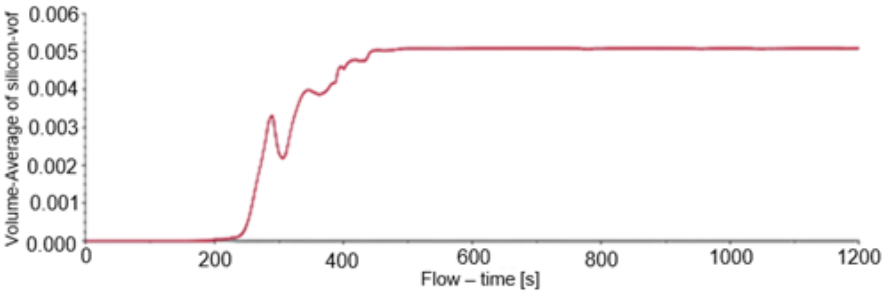

(b)

Figure 3 – Temporal evolution of gas and solid particle concentrations in the $CO_2 + 0.005\,Si - N_2$ system at $p = 0.1$ MPa and $T = 300$ K: a) CO_2 mole fraction; b) Si volume fraction.

4. CONCLUSION

This study presented a numerical investigation of diffusion-convective mass transfer in the $CO_2 - Si - N_2$ gas–aerosol system at a very low solid-phase volume fraction of $\phi = 0.5\%$ under isothermal and isobaric conditions. Simulations were conducted in ANSYS Fluent using a combined approach integrating the Species Transport equations with the Eulerian Multiphase Flow method.

The results establish that even at this low particle loading, the system behaves in a manner qualitatively distinct from a pure gas mixture. Gravitational settling of Si particles onto the bottom wall of the upper vessel produces a local density inversion that, at $t \approx 100 - 105$ s, crosses the threshold for convective instability and triggers a flow restructuring consistent with the Rayleigh–Taylor mechanism. This transition is evidenced by a sharp acceleration in CO_2 gas-phase transport and the appearance of pronounced oscillations in the Si volume fraction, indicative of intermittent, non-stationary dispersed-phase migration. The formation of a teardrop-shaped solid-phase structure in the

lower vessel at $t \approx 280$ s provides morphological confirmation of the RT instability.

A key outcome of this work is the demonstration that the two phases follow fundamentally different transport pathways: CO_2 is transferred smoothly and continuously via a diffusion-convective mechanism, whereas Si migrates through a succession of discrete convective pulses. This divergence stems from a deep asymmetry in the inertial characteristics of the phases and their respective responses to the gravitational field.

The combined Species Transport and Eulerian Multiphase model proves applicable to diffusion-convective processes in dilute gas–solid systems without recourse to empirical corrections. These findings carry practical relevance for assessing conditions under which even trace concentrations of a dispersed phase can substantially alter the mass transfer regime — notably in the design of experiments targeting mutual diffusion coefficient measurements in gas–aerosol systems.

Future work should address a systematic parametric study across the range $\phi = 0 - 5\%$ to identify the critical loading ϕ_{cr} below which solid-phase effects on gas-phase transport become negligible, alongside extension of the model to three-dimensional geometry and incorporation of heat transfer effects.

REFERENCES

1. Kosov, V. N. and V. D. Seleznev. *Anomalous Occurrence of Free Gravitational Convection in Isothermal Ternary Gas Mixtures*. Ekaterinburg, Russia: Ural Branch of the Russian Academy of Sciences, 2004.
2. Dil'man, V. V., D. A. Lipatov, V. A. Lotkhov, and et al. "Instability in unsteady-state evaporation of binary solutions into an inert gas." *Theoretical Foundations of Chemical Engineering* 39, no. 6 (2005): 566–572.
3. Kaminskii, V. A. "Special modes of three-component diffusion in gases." *Russian Journal of Physical Chemistry A* 85, no. 12 (2011): 2203–2208.
4. Kosov, V. N., Y. I. Zhavrin, and V. D. Seleznev. "Inversion of the density gradient and the 'gate' in isothermal mixing of gases." *Technical Physics* 43, no. 5 (1998): 488–492.
5. Zhavrin, Y. I., V. Kosov, D. Kul'zhanov, and K. Karataeva. "Effect of the pressure on the type of mixing in a three-component gas mixture containing a component possessing the properties of a real gas." *Technical Physics Letters* 26, no. 12 (2000): 1108–1109.
6. Kosov, V. N., O. V. Fedorenko, Y. I. Zhavrin, and V. Mukamedenkyzy. "Instability of mechanical equilibrium during diffusion in a three-component gas mixture in a vertical cylinder." *Technical Physics* 59, no. 4 (2014): 482–486.
7. Zhussanbayeva, A., V. N. Kossov, O. V. Fedorenko, and M. Zhaneli. "Instability of mechanical equilibrium and concentration convection in isothermal ternary gaseous systems." *Physical Sciences and Technology* 9, no. 1-2 (2022): 55–61.
8. Moldabekova, M., V. Mukamedenkyzy, M. Asembayeva, and A. Tolepbergen. "Investigation of the diffusion of two gases equally diluted with different ballast gases." *Recent Contributions to Physics* 89, no. 2 (2024): 57–61.
9. Kossov, V. N. and H. Altenbach. "Diffusion mechanisms of convective instability in liquid and gas mixtures." *Journal of Applied Mathematics and Mechanics / ZAMM* 103, no. 11 (2023): e202300801.
10. Banerjee, A. "Rayleigh-taylor instability: A status review of experimental designs and diagnostics." *Journal of Fluids Engineering* 142, no. 12 (2020): 120801.
11. Balachandar, S. and J. K. Eaton. "Turbulent dispersed multiphase flow." *Annual review of fluid mechanics* 42, no. 1 (2010): 111–133.
12. Capecelatro, J. and et al. "Gas-particle dynamics in high-speed flows: A review." *Annual Review of Fluid Mechanics* 56 (2024): 379–403.
13. Villafañe, L., A. Aliseda, S. Ceccio, P. Di Marco, N. Machicoane, and T. J. Heindel. "Experimental methods for dispersed multiphase flows." *International Journal of Multiphase Flow* 189 (2025): 105239.
14. Yan, Y., K. Mohanarangam, W. Yang, and J. Tu. "Experimental measuring techniques for industrial-scale multiphase flow problems." *Experimental and Computational Multiphase Flow* 6 (2024): 1–13.
15. Bolegenova, S., A. Askarova, S. Ospanova, and et al. "Technology of reducing greenhouse gas emissions." *Physical Sciences and Technology* 11, no. 1-2 (2024): 64–75.
16. Tas-Koehler, S. and et al. "A critical analysis of drag force modelling for disperse gas-solid flows." *Chemical Engi-*

neering Science (2021): 117007.

17. Akula, B. and D. Ranjan. "Dynamics of buoyancy-driven flows at moderately high Atwood numbers." *Journal of Fluid Mechanics* 795 (2016): 313–355.
18. Liang, Y., K. Alkindi, K. Alzeyoudi, L. Liu, M. Ali, and N. Masmoudi. "Experimental investigation of three-dimensional Rayleigh-Taylor instability." *Journal of Fluid Mechanics* 994 (2024): A7.
19. Liu, C., Y. Zhang, and Z. Xiao. "Unified model for Rayleigh-Taylor and Richtmyer-Meshkov fingers." *Journal of Fluid Mechanics* 954 (2023): A13.
20. Peixoto, M. L. R., M. S. C. A. Brito, R. J. Santos, and V. J. P. Vilar. "Kinetic model implementation in raceway pond reactors." *Chemical Engineering Research and Design* 210 (2024): 150–162.
21. Pancorbo, P. M., J. M. Ortiz de Zárate, H. Bataller, and F. Croccolo. "Gravity effects on Soret-induced fluctuations." *European Physical Journal E* 40, no. 2 (2017): 22.
22. Kossov, V. N., V. Mukamedenkyzy, A. Tolepbergen, and H. Altenbach. "Peculiarities of combined mixing caused by instability of mechanical equilibrium." *International Journal of Chemical Engineering* (2025): 9643371.
23. Mukamedenkyzy, V. and A. Tolepbergen. "Some features of Rayleigh-Taylor convection in the mixing of ideal gas mixtures." *Recent Contributions to Physics* 92, no. 1 (2025): 110–119.
24. ANSYS, Inc., "ANSYS Fluent Theory Guide 2025 R1." ANSYS Documentation, 2025, accessed: November 2025.

Information about authors

V. Mukamedenkyzy *– Candidate of Physical and Mathematical Sciences, Associate Professor of the Department of Thermal Physics and Technical Physics, Al-Farabi Kazakh National University, Almaty, Kazakhstan, email: mukamedenkyzyvenera@gmail.com,*
A. Tolepbergen *– student of Department of Thermal Physics and Technical Physics, Al-Farabi Kazakh National University, Almaty, Kazakhstan, e-mail: arsen4236@gmail.com .*

IRSTI 29.15.19 https://doi.org/10.51889/IJAPA.2026.1.1.004

RESONANCE STRUCTURE OF THE ^{7}Be NUCLEUS IN MICROSCOPIC TWO-CLUSTER MODEL

V. Kurmangaliyeva[1*], O. Agyl-Mussapar[1], N. Kalzhigitov[1], B. Massak[1] and S. Amangeldinova[1]

[1] *Al-Farabi Kazakh National University, Almaty, Kazakhstan*

*Corresponding Author: venera_baggi@mail.ru

Received 22 May 2026; Accepted 4 June 2026

Abstract. The resonant structure of the light nucleus ^{7}Be in the $^4_2$He $+^3_2$ He cluster configuration has been investigated within the framework of a microscopic two-cluster model employing the algebraic version of the resonating group method. Elastic scattering cross sections for the reaction $^7_4$Be $\rightarrow ^4_2$He $+ ^3_2$He are calculated and the corresponding energy dependence is obtained. The total elastic scattering cross sections are calculated using the modified nucleon–nucleon Hasegawa–Nagata potential. The obtained resonance parameters for the available states $\frac{1}{2}^-$, $\frac{3}{2}^-$, $\frac{5}{2}^-$, and $\frac{7}{2}^-$ are determined and compared with experimental data. The resonance parameters for the $\frac{5}{2}^-$ and $\frac{7}{2}^-$ states are also obtained, indicating the presence of broad and narrow resonances, which indicates the existence of both short-lived and long-lived states in the nuclear system under study.

Keywords: cluster model, Resonating Group Method, resonance states, elastic scattering, nucleon–nucleon interaction, modified Hasegawa–Nagata potential.

1. INTRODUCTION

Nuclear physics, as well as nuclear astrophysics, continues to consider the study of the structure of light nuclei as one of its central and highly relevant problems. Light nuclear systems provide valuable information about the properties of nuclear forces and the mechanisms of nuclear reactions. In particular, the investigation of resonance states in light nuclei plays an important role in understanding the interaction between nuclear clusters and the dynamics of nuclear systems.

The ^{7}Be nucleus attracts considerable interest due to its cluster structure and its role in various nuclear processes. Many theoretical and experimental studies have been devoted to the investigation of its energy spectrum and resonance properties [1, 2, 3]. The cluster approach has proven to be an effective tool for describing light nuclei, where the nucleus is considered as a system of interacting clusters. Such models allow a physically transparent interpretation of the structure of nuclear states and the nature of resonances [4, 5, 6, 7, 8, 9].

In particular, the ^{7}Be nucleus can be described within the two-cluster configuration $^4_2$He $+ ^3_2$He. This configuration is especially suitable for studying the resonance structure and scattering processes in this system. Various theoretical methods have been applied to analyze these states, including the Resonating Group Method (RGM) [10]. In the present work the resonance structure of the ^{7}Be nucleus is investigated within the microscopic two-cluster model using the algebraic version of the Resonating Group Method (AV RGM) [8, 11]. The resonance parameters for several negative-parity states are determined and compared with available experimental data [3].

2. THEORETICAL MODEL

To describe various bound and excited states of atomic nuclei in a microscopic two-cluster representation, we apply the AV RGM. The full set of generator functions is used to describe the relative motion of clusters both in connected states and in a continuum, which is a key feature of this method.

Within this approach, the wave function of a two-cluster system can be expressed in the following form [12]:

$$\Psi_J = \widehat{\mathscr{A}}\left\{[\varphi_1(A_1)\varphi_2(A_2)]_s\,\psi^J_{LS}(\vec{q})\right\} \tag{1}$$

where $\varphi_1(A_1)$ is the internal wave function of the first cluster consisting of A_1 nucleons, and $\varphi_2(A_2)$ is the internal wave function of the second cluster consisting of A_2 nucleons. Both functions depend on the spatial, spin, and isospin coordinates of individual nucleons and are antisymmetric with respect to permutations of nucleons within each cluster. In the RGM, these internal functions are assumed to be known. In this approach, the wave function of a two-cluster system is constructed using a complete set of generator functions, enabling the description of cluster relative motion in both bound and continuum states. The function $\psi^J_{LS}(\vec{q})$ is a solution of the dynamical equation and depends on the Jacobi coordinate vector $\vec{q}$, which defines the relative distance between the clusters.

Within the algebraic version of the Resonating Group Method, the wave function $\psi^J_{LS}(\vec{q})$ is expanded into an infinite series of three-dimensional harmonic oscillator functions $\psi_{nL}(q,r_0)$:

$$\psi^J_{LS}(\vec{q}) = \sum_{n=n_0}^{\infty} C_{nL}\psi_{nL}(q,r_0) \tag{2}$$

where C_{nL} are the expansion coefficients and q is the magnitude of the Jacobi vector. The explicit form of the oscillator functions $\psi_{nL}(q,r_0)$ can be found in Ref. [12]. Since the oscillator functions form an orthonormal basis, the wave function of any two-cluster system can be expanded in terms of these functions.

Taking into account (1) and (2), within the algebraic version of the RGM the total wave function of the two-cluster system can be represented as a generalized Fourier series:

$$\Psi_J = \sum_{n=n_0}^{\infty} C_{nL}\Psi_{nL} \tag{3}$$

This leads to the following system of algebraic equations for the expansion coefficients:

$$\sum_{m=n_0}^{\infty}\left[\langle\vec{n}L|\widehat{H}|\vec{m}L\rangle - E\,\delta_{n,m}\right]C_{mL} = 0 \tag{4}$$

where $\widehat{H}$ is the Hamiltonian of the nuclear system and E is the total energy. The function

$$\Psi_{nL} = \widehat{\mathscr{A}}\{\varphi_1(A_1)\varphi_2(A_2)\psi_{nL}(q,b)Y_{LM}(\vec{q})\} \tag{5}$$

represents the many-body oscillator function of the cluster system.

3. INTERACTION POTENTIAL

In the present work, the nucleon–nucleon interaction is described using the modified Hasegawa–Nagata potential (MHNP) [13, 14].

The MHNP provides a more detailed description of nucleon–nucleon interactions by including central, spin–orbit, and Coulomb components. The Hamiltonian of the system is written as

$$\widehat{H} = \widehat{T} + \widehat{V} \tag{6}$$

where the kinetic energy operator is defined in the center-of-mass frame.

The potential energy is represented as a sum of three contributions:

$$\widehat{V} = \sum_{j>i=1}^{A} \widehat{V}^{(\mathrm{cn})}(ij) + \sum_{j>i=1}^{A} \widehat{V}^{(\mathrm{so})}(ij) + \sum_{j>i=1}^{A} \widehat{V}^{(\mathrm{c})}(ij) \tag{7}$$

where $\widehat{V}^{(\mathrm{cn})}$ is the central interaction, $\widehat{V}^{(\mathrm{so})}$ is the spin–orbit interaction, and $\widehat{V}^{(\mathrm{c})}$ is the Coulomb interaction.

The central part of the interaction is expressed using spin–isospin projectors:

$$\widehat{V}^{(\mathrm{cn})}(ij) = \sum_{S=0,1} \sum_{T=0,1} V^{(\mathrm{cn})}_{2S+1,2T+1}(ij) \widehat{P}_S(ij) \widehat{P}_T(ij) \tag{8}$$

where S and T are the spin and isospin of the two-nucleon system.

The radial dependence of the nucleon–nucleon interaction depends on the spin and isospin channels and is represented as a superposition of Gaussian functions:

$$V^{(\nu)}_{2S+1,2T+1}(r_{ij}) = \sum_{i=1}^{N_G} V^{(\nu,i)}_{2S+1,2T+1} \exp\left\{ - \left(\frac{r_{ij}}{a^{(\nu,i)}_{2S+1,2T+1}} \right)^2 \right\} \tag{9}$$

where $V^{(\nu,i)}_{2S+1,2T+1}$, $a^{\nu,i}_{2S+1,2T+1}$ are the strength and range parameters of the interaction. The index ν specifies the type of interaction (central or spin–orbit).

4. Results and Discussions

Within the cluster approximation, the ^{7}Be nucleus is considered as a two-cluster system:

$$^7_4\mathrm{Be} = ^4_2\mathrm{He} + ^3_2\mathrm{He} \tag{10}$$

To perform all necessary calculations within the model, the oscillator length (b), which is the only free parameter, is determined by minimizing the energy of the two-cluster threshold. To achieve agreement with experimental data, the Majorana parameter Δm is slightly adjusted.

The optimal values of the input parameters (oscillator length b and Majorana parameter Δm) are presented in Table 1.

Table 1. Input parameters used in the calculations

Nucleus	b**, fm**	Δm	f_{LS}
$^7_4$Be	1.362	0.0002	1.000

It was also found that the spin–orbit component of the modified Hasegawa–Nagata potential is excessively strong and leads to nonphysical results. To avoid this issue, a scaling factor f_{LS} was introduced for the spin–orbit interaction and treated as a variational parameter [14]. Let us consider

the elastic scattering cross sections for the reaction $^7_4\mathrm{Be} \to {}^4_2\mathrm{He} + {}^3_2\mathrm{He}$ for different nuclear states of the ^{7}Be nucleus.

Figure 1 shows the energy dependence of the elastic scattering cross section obtained using the MHNP.

As can be seen from Fig.1, resonance states are observed for $J^\pi = \frac{5}{2}^-$ and $J^\pi = \frac{7}{2}^-$. This indicates that the excitation of a neutron from the $p_{3/2}$ shell to the $f_{5/2}$ and $f_{7/2}$ states leads to the formation of resonance states.

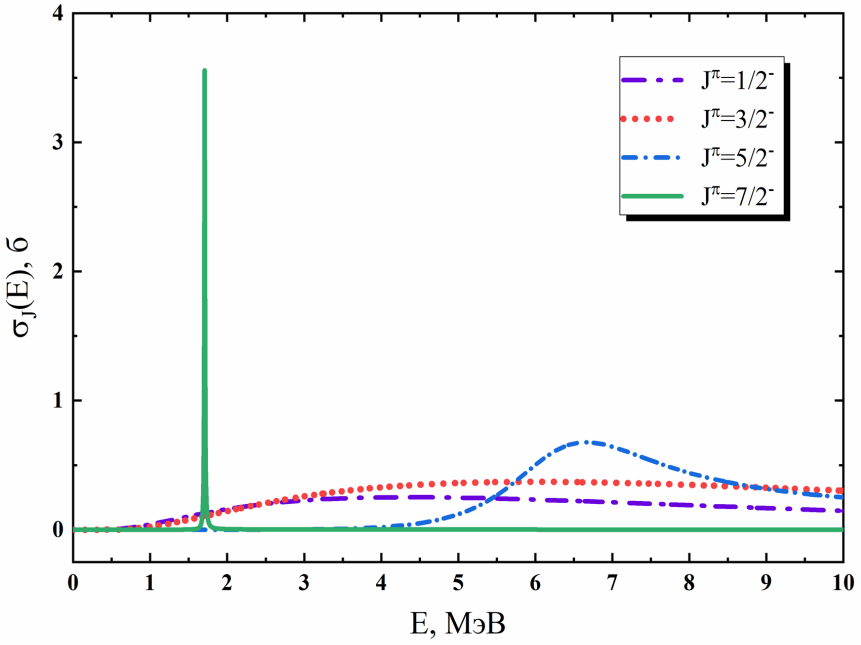

Figure 1 – Energy dependence of the elastic scattering cross section σ_J for the reaction $^7_4\mathrm{Be} \to {}^4_2\mathrm{He} + {}^3_2\mathrm{He}$ obtained with the MHNP.

The presence of narrow and broad resonances in the calculated cross sections reflects different physical mechanisms. Narrow resonances, such as the $\frac{7}{2}^-$ state, correspond to relatively long-lived states with small decay widths, indicating a more stable configuration of the cluster system. On the other hand, broad resonances, such as the $\frac{5}{2}^-$ state, are characterized by larger widths and shorter lifetimes, which indicates stronger coupling to the continuum. The resonances are observed within a relatively narrow energy interval; therefore, the energy range from 0 to 10 MeV was considered in the calculations. Depending on the resonance width Γ, the resonances can be classified as broad or narrow. The $J^\pi = \frac{5}{2}^-$ state corresponds to a broad resonance with a width of $\Gamma = 2.452$ MeV, while the $J^\pi = \frac{7}{2}^-$ state exhibits a sharp peak with a width of $\Gamma = 0.012$ MeV, indicating a narrow resonance.

Table 2. presents the resonance parameters of the ^{7}Be nucleus obtained using the modified Hasegawa–Nagata potential, where E denotes the resonance energy, Γ is the resonance width, and the experimental values are taken from reference [3].

Table 2. Resonance parameters of the ^{7}Be nucleus

J^π	E, MeV (MHNP)	Γ, MeV (MHNP)	E, MeV (exp.) [3]	Γ, MeV (exp.) [3]
$\frac{5}{2}^-$	6.242	2.452	5.143 ± 0.10	1.2
$\frac{7}{2}^-$	1.709	0.012	2.98 ± 50	0.175 ± 7

The results also confirm that the $\frac{1}{2}^-$ and $\frac{3}{2}^-$ states correspond to bound states of the system. As shown in Table 3, the good agreement of the calculated energies with experimental data, especially for the modified Hasegawa–Nagata potential, confirms the validity of the $^4_2$He $+ ^3_2$He cluster description of the ^{7}Be nucleus.

Table 3. Bound states of the ^{7}Be nucleus

J^π	E, MeV (MHNP)	E, MeV (exp.) [3]
$\frac{1}{2}^-$	-0.306	—
$\frac{3}{2}^-$	-1.587	-1.588

Overall, the analysis shows that the spin–orbit interaction plays a crucial role in the correct description of resonance states in light nuclei, and its inclusion significantly improves the agreement between theoretical and experimental results.

5. Conclusion

In this work, the resonance structure of the ^{7}Be nucleus has been studied within the microscopic two-cluster model using the $^4_2$He $+ ^3_2$He configuration. The resonance states $J^\pi = \frac{5}{2}^-$ and $J^\pi = \frac{7}{2}^-$ were identified, corresponding to broad and narrow resonances, respectively.

It was also shown that the $J^\pi = \frac{1}{2}^-$ and $J^\pi = \frac{3}{2}^-$ states are bound states, whose energies are in good agreement with experimental data. The comparison of different nucleon–nucleon potentials demonstrates that the modified Hasegawa–Nagata potential provides a more accurate description of the system.

Overall, the results confirm the validity of the cluster approach for describing the structure of the ^{7}Be nucleus.

References

1. Toshitaka, K., M. Takehiro, and A. Akito. “Electromagnetic properties of ^{7}Li and ^{7}Be in a cluster model.” 413, no. 2 (1984): 323–352.
2. Varga, K., Y. Suzuki, K. Arai, and Y. Ogawa. “Microscopic description of light unstable nuclei with the stochastic variational method.” 616, no. 1 (1997): 383–393.
3. Tilley, D. R., C. M. Cheves, J. L. Godwin, G. M. Hale, H. M. Hofmann, J. H. Kelley, C. G. Sheu, and H. R. Weller. “Energy levels of light nuclei /A=5, 6, 7.” 708, no. 1 (2002): 3–163.
4. Wildermuth, K. and W. McClure. *Cluster Representations of Nuclei*. 1966, 41.
5. Fujiwara, Y., H. Horiuchi, K. Ikeda, M. Kamimura, K. Katō, Y. Suzuki, and E. Uegaki. “Chapter II. \Comprehensive Study of Alpha-Nuclei.” *Progress of Theoretical Physics Supplement* 68 (1980): 29–192.

6. Horiuchi, H., K. Ikeda, and Y. Suzuki. “Chapter III. Molecule-Like structures in nuclear system.” *Progress of Theoretical Physics Supplement* 52 (1972): 89–172.
7. Horiuchi, H. and K. Ikeda. “Cluster model of the nucleus.”*In* , edited by Y. Akaishi, S. A. Chin, and K. Ikeda, 258. World Scientific, 1987.
8. Filippov, G. F. and I. Okhrimenko. “Use of an oscillator basis for solving continuum problems.” *Soviet Journal of Nuclear Physics* 32 (1981): 480–484, (in Russ.).
9. Filippov, G. F., V. S. Vasilevsky, and L. L. Chopovsky. “Solution of problems in the microscopic theory of the nucleus using the technique of generalized coherent states.” *Soviet Journal of Particles and Nuclei* 16 (1985): 153–177, (in Russ.).
10. Wheeler, J. A. “On the mathematical description of light nuclei by the method of resonating group structure.” *Physical Review* 52 (1937): 1107–1122.
11. Filippov, G. F. “On taking into account correct asymptotic behavior in oscillator-basis expansions.” *Soviet Journal of Nuclear Physics* 33 (1981): 488–489, (in Russ.).
12. Lashko, Y., G. Filippov, and V. Vasilevsky. “Dynamics of two-cluster systems in phase space.” *Nuclear Physics A* 941 (2015): 121–144.
13. Hasegawa, A. and S. Nagata. “Ground state of ^{6}Li.” *Progress of Theoretical Physics* 45 (1971): 1786–1807.
14. Tanabe, F., A. Tohsaki, and R. Tamagaki. “α-α scattering at intermediate energies.” *Progress of Theoretical Physics* 53 (1975): 677–691.

Information about authors

Venera Kurmangaliyeva *– Candidate of Physical and Mathematical Sciences, Associate Professor, Faculty of Physics and Technology, Al-Farabi Kazakh National University, Almaty, Kazakhstan. e-mail: venera_baggi@mail.ru,*

Orazbay Agyl-Mussapar *– PhD Student, Faculty of Physics and Technology, Al-Farabi Kazakh National University, Almaty, Kazakhstan. e-mail: oagilmuzaffar@gmail.com,*

Nursultan Kalzhigitov *– PhD, Faculty of Physics and Technology, Al-Farabi Kazakh National University, Almaty, Kazakhstan. e-mail: knurtol@gmail.com,*

Bekarys Massak *– PhD Student, Faculty of Physics and Technology, Al-Farabi Kazakh National University, Almaty, Kazakhstan. e-mail: bekarysbereketov@gmail.com,*

Sabina Amangeldinova *– PhD Student, Faculty of Physics and Technology, Al-Farabi Kazakh National University, Almaty, Kazakhstan. e-mail: sabinaa247@gmail.com.*

IRSTI 44.39.29 https://doi.org/10.51889/IJAPA.2026.1.1.005

DEVELOPMENT OF AN EXCITATION CONTROL ALGORITHM FOR INCREASING THE EFFICIENCY OF SMALL WIND TURBINE GENERATORS

F.N. Bulatbayev[1], **Y.F. Bulatbayeva**[1] **and A.M. Bolatov**[1*]

[1] *Abylkas Saginov Karaganda Technical University, Karaganda, Kazakhstan*

*Corresponding Author: abylabolatov@gmail.com

Received 18 May 2026; Accepted 4 June 2026

Abstract. This paper presents the development and investigation of an excitation-current-based control approach for improving voltage stabilization and operating performance of a small-scale wind energy conversion system operating under variable wind speed conditions. The proposed system employs a synchronous generator with regulated excitation integrated into a subsystem-oriented MATLAB/Simulink simulation model intended for analysis of aerodynamic and electromechanical operating processes. A mathematical model of the wind energy conversion system was developed considering aerodynamic power conversion, synchronous generator electromechanical dynamics, excitation current regulation, and electrical loading conditions. A PI/PID-based excitation control algorithm was implemented for continuous adjustment of excitation current according to generator terminal voltage deviations under transient wind operating modes. Simulation studies were performed under different wind speed and loading conditions in order to investigate generated voltage, electrical power, excitation current, and rotor rotational speed characteristics. The obtained results demonstrated that excitation-current regulation improves voltage stabilization performance, reduces transient voltage oscillations, and enhances operating stability of the generating system under stochastic wind disturbances. The developed control approach also improved adaptation of the synchronous generator to variable mechanical loading conditions and reduced the influence of aerodynamic disturbances on electromechanical operating behavior. The proposed excitation-based regulation method represents a practically applicable and comparatively low-complexity approach for improving the operating efficiency and voltage stabilization characteristics of small-scale wind energy conversion systems.

Keywords: Wind energy conversion system; synchronous generator; excitation current control; voltage stabilization; MATLAB/Simulink; PID controller; small-scale wind turbine.

1. INTRODUCTION

The rapid development of renewable energy technologies has significantly increased the role of wind energy in modern electrical power systems. According to the Global Wind Report 2025, 117 *GW* of new wind power capacity was installed worldwide in 2024, increasing the cumulative global wind capacity to 1136 *GW* [1]. The continuous growth of renewable energy capacity demonstrates the increasing importance of environmentally sustainable and low-carbon electricity generation technologies in the global energy sector [2].

Modern wind energy conversion systems are considered among the most promising technologies for distributed and autonomous electricity generation. Wind energy is widely available in many regions of the world and possesses considerable long-term potential for sustainable power supply applications [3]. Regions characterized by favorable wind conditions are especially attractive for the deployment of small-scale and autonomous wind power systems operating independently or as part of hybrid renewable energy complexes [4].

The operational efficiency of wind turbine generators strongly depends on wind speed conditions. The stochastic nature of wind flow causes fluctuations in turbine rotational speed and generated electrical power, which negatively affect the stability and operating characteristics of wind energy

conversion systems [5]. In practical operating conditions, unstable wind speed may lead to voltage fluctuations, deterioration of generated power quality, and reduction of electromechanical energy conversion efficiency [6]. In addition, stable operation of wind turbine generators under continuously changing mechanical loads remains one of the important engineering problems in modern wind power systems [7].

Various generator configurations are currently applied in wind energy conversion systems, including synchronous and induction generator systems [8]. Variable-speed wind turbine generators provide improved operational flexibility and more efficient adaptation to changing wind conditions compared with fixed-speed operating systems [9]. The application of synchronous and induction generators in wind turbine systems makes it possible to improve the regulation characteristics and operational efficiency of electrical power generation under variable operating conditions [10].

One of the promising approaches for improving the operating characteristics of wind turbine generators is the application of excitation current control systems. Regulation of generator excitation allows stabilization of operating modes, improvement of voltage characteristics, and enhancement of power generation efficiency under variable wind speed conditions. However, maintaining stable operating characteristics of small-scale wind energy conversion systems under continuously changing aerodynamic conditions remains a significant engineering challenge.

The main contribution of this study consists in the development of an excitation-current-based control structure for improving voltage stabilization and operational stability of a small-scale wind energy conversion system under variable wind speed conditions. In contrast to conventional fixed-excitation operating approaches, the proposed system employs continuous excitation current regulation of a synchronous generator integrated into a subsystem-oriented MATLAB/Simulink model of the wind energy conversion system. The developed approach enables investigation of the interaction between aerodynamic disturbances, generator electromechanical operating behavior, and excitation-based voltage stabilization processes under transient wind operating conditions.

The aim of this study is to develop and investigate an excitation control algorithm for a synchronous generator with regulated excitation in order to improve the efficiency and operational stability of a small-scale wind energy conversion system operating under variable wind speed conditions.

2. System Description and Mathematical Model

2.1. Structure of the Wind Energy Conversion System

The developed wind energy conversion system is based on the application of a synchronous generator with regulated excitation operating under variable wind speed conditions. The general functional structure of the proposed system includes a wind turbine, a synchronous generator, an excitation control system, a rectifier unit, a DC link, and an electrical load, as shown in Figure 1.

The wind turbine converts the kinetic energy of the airflow into mechanical rotational energy transmitted to the generator shaft. Variations in wind speed cause continuous changes in the rotational speed and electromagnetic operating conditions of the generating system. Under such operating conditions, stable voltage regulation and maintenance of generator operating characteristics become important tasks for small-scale wind energy systems.

Excitation systems of synchronous machines include excitation control elements, voltage measurement units, excitation regulation subsystems and additional stabilizing components that ensure stable operation of the synchronous machine in dynamic operating modes [11]. The excitation system structure is formed using voltage feedback signals obtained from the generator terminal conditions and excitation regulating elements responsible for the stabilization of generator operating modes.

The excitation control subsystem performs regulation of the generator magnetic field by control-

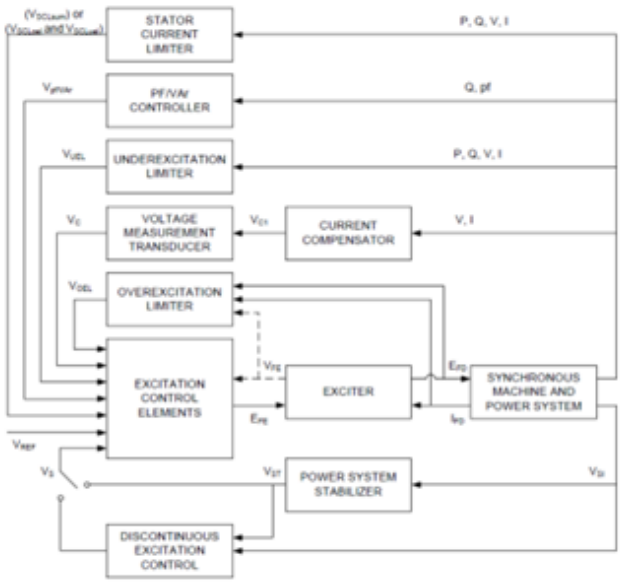

Figure 1 – Functional structure of the proposed wind energy conversion system

ling the excitation current supplied to the field winding of the synchronous generator. Regulation of the excitation current allows stabilization of generator terminal voltage and improvement of operating characteristics under continuously changing mechanical loading conditions caused by wind speed fluctuations.

According to IEEE excitation system representation principles, excitation control structures may include voltage transducers, excitation regulators, stabilizing elements, and supplementary feedback loops used for maintaining stable synchronous machine operation under transient operating conditions [11]. In the proposed wind energy conversion system, voltage feedback from the generator output is used as the main control signal for excitation current regulation.

The electrical energy generated by the synchronous generator is transferred through a rectifier and DC link to the electrical load. The developed system structure provides the possibility of investigating the influence of excitation current regulation on voltage stabilization, generated power characteristics, and operational efficiency of the wind energy conversion system under variable wind speed conditions.

2.2. Synchronous Generator with Regulated Excitation

The operating performance of small-scale wind energy conversion systems is strongly influenced by variable wind speed conditions causing continuous changes in turbine rotational speed and generator electromechanical operating modes. Under such conditions, conventional generating systems operating without effective excitation regulation may experience voltage instability, deterioration of generated power characteristics, and reduction of energy conversion efficiency.

In synchronous generators, the electromagnetic operating state is determined by the interaction between the rotor magnetic field and stator electromagnetic processes. The magnetic field of the rotor is created by the excitation winding supplied with direct current, while the generated electromotive force depends on the excitation current magnitude and magnetic flux distribution inside the machine [12]. Therefore, excitation current variation directly influences generator terminal voltage, reactive power characteristics, and dynamic operating behavior.

One of the important advantages of synchronous generators in wind energy applications is the

possibility of active control of electromagnetic operating conditions through excitation current regulation. Unlike fixed-excitation operating modes, regulated excitation systems allow adaptation of generator operating characteristics to continuously changing wind conditions. Under variable mechanical torque conditions caused by wind speed fluctuations, excitation regulation provides compensation of voltage deviations and improves stabilization of generator operating parameters.

According to modern excitation control principles, excitation systems play an important role not only in voltage regulation but also in maintaining electromechanical stability and improving transient operating performance of synchronous generating systems [12]. Fast excitation response allows the generating system to maintain more stable operating conditions during disturbances and rapidly changing mechanical loading modes.

For small-scale wind energy systems, the application of regulated excitation becomes especially important due to the stochastic nature of wind flow and increased sensitivity of low-power systems to voltage fluctuations. In such operating conditions, excitation current control may significantly influence voltage stabilization characteristics and the overall efficiency of electrical energy conversion.

Therefore, in the proposed wind energy conversion system, a synchronous generator with regulated excitation is used as the main generating unit. The excitation subsystem performs continuous excitation current adjustment according to generator operating conditions, providing improved voltage stabilization and more stable operation of the generating system under variable wind speed conditions.

2.3. Mathematical Model of the Wind Turbine Generator

The mathematical model of the developed wind energy conversion system is based on the electromechanical relationships describing the interaction between the wind turbine mechanical subsystem and the synchronous generator electromagnetic subsystem. The developed model is intended for investigation of the influence of excitation current regulation on voltage stabilization and operating characteristics of the generating system under variable wind speed conditions.

The mechanical power extracted from the wind flow by the wind turbine is determined by the following expression:

$$P_m = \frac{1}{2}\rho A v_w^3 C_p(\lambda, \beta) \tag{1}$$

where P_m is the mechanical power of the wind turbine, ρ is the air density, A is the turbine swept area, v_w is the wind speed, and $C_p(\lambda, \beta)$ is the aerodynamic power coefficient of the wind turbine.

According to (1), the generated mechanical power strongly depends on wind speed variations due to the cubic relationship between wind velocity and extracted aerodynamic power. Therefore, changes in wind speed directly influence the mechanical torque transmitted to the synchronous generator shaft and affect the electromechanical operating conditions of the generating system.

The electromechanical dynamics of the synchronous generator are determined by the balance between the mechanical torque produced by the wind turbine and the electromagnetic torque developed by the generator. According to synchronous machine dynamic principles, the rotor motion equation may be represented as follows [13]:

$$J\frac{d\omega}{dt} = T_m - T_e - B\omega \tag{2}$$

where J is the rotor moment of inertia, ω is the angular rotational speed, T_m is the mechanical torque produced by the wind turbine, T_e is the electromagnetic torque of the synchronous generator, and B is the damping coefficient.

Under variable wind speed conditions, fluctuations of the mechanical torque lead to changes in rotor speed and generator electromechanical operating parameters. Such operating conditions may cause voltage instability and deterioration of generated power characteristics, especially in small-scale wind energy systems operating under continuously changing mechanical loading conditions.

The generated electromotive force of the synchronous generator depends on the magnetic flux created by the excitation system and rotor rotational speed. The relationship between generated electromotive force and excitation conditions may be expressed as:

$$E = k\Phi\omega \tag{3}$$

where E is the generated electromotive force, k is the machine constant, Φ is the magnetic flux created by the excitation winding, and ω is the angular rotational speed of the rotor.

According to (3), excitation current variation directly affects the magnetic flux of the synchronous generator and influences the generated electromotive force and terminal voltage characteristics. Therefore, excitation current regulation becomes one of the main control mechanisms for stabilization of generator operating conditions under variable wind speed modes.

The developed mathematical relationships form the basis for implementation of the excitation control algorithm and further simulation studies of the wind energy conversion system in the MATLAB/Simulink environment.

2.4. Excitation System Model

The excitation system developed for the proposed wind energy conversion system is intended for continuous regulation of the synchronous generator excitation current under variable wind speed operating conditions. The excitation subsystem performs stabilization of generator operating characteristics by controlling the magnetic field of the synchronous generator according to changes in generator terminal voltage and electromechanical operating conditions.

In the developed model, the generator terminal voltage is used as the main feedback signal for the excitation control subsystem. Variations in wind speed and mechanical loading conditions cause changes in generator operating parameters and voltage characteristics. The excitation control subsystem continuously monitors generator voltage conditions and forms the required excitation control action for stabilization of the generating system operating mode.

The excitation control process is based on continuous adjustment of the excitation current supplied to the rotor field winding of the synchronous generator. Under reduced generator terminal voltage conditions, the excitation subsystem increases the excitation current to strengthen the magnetic field and compensate voltage deviations. Conversely, under increased voltage conditions, the excitation current is reduced to maintain stable generator operating characteristics.

The developed excitation system model provides adaptive response of the generating system to continuously changing wind speed conditions and electromechanical operating modes. Excitation current regulation improves voltage stabilization characteristics and reduces the influence of wind speed fluctuations on generator operating performance.

The developed excitation subsystem is integrated into the mathematical model of the wind energy conversion system and forms the basis for implementation of the excitation control algorithm in the MATLAB/Simulink environment. The proposed excitation system structure provides the possibility of investigating the influence of excitation current regulation on generated voltage stability and operational efficiency of the small-scale wind energy conversion system.

3. Excitation Control Algorithm

3.1. Principles of Excitation Current Regulation

One of the main operating challenges of small-scale wind energy conversion systems is the instability of generator operating conditions under variable wind speed modes. Wind speed fluctuations continuously affect turbine rotational speed and mechanical torque transmitted to the synchronous generator shaft, resulting in variations of generator voltage and generated electrical power. Under such operating conditions, maintaining stable voltage characteristics becomes one of the key tasks of the generating system control process.

In synchronous generators, the excitation current directly determines the rotor magnetic flux and significantly influences the generated electromotive force and terminal voltage characteristics. Therefore, excitation current regulation may be used as an effective control mechanism for stabilization of generator operating conditions under continuously changing wind energy input conditions [14].

Unlike fixed-excitation operating modes, regulated excitation systems provide adaptive adjustment of generator electromagnetic operating parameters according to changes in generator terminal voltage and electromechanical operating conditions. In modern wind energy systems, excitation current regulation is considered one of the important approaches for improving voltage stabilization characteristics and increasing operational stability under transient operating modes.

The proposed control approach is based on continuous monitoring of generator terminal voltage and dynamic adjustment of excitation current according to voltage deviation conditions. Under reduced voltage conditions caused by decreasing wind speed or increased loading, the excitation subsystem increases excitation current in order to strengthen the rotor magnetic field and compensate voltage deviations. Conversely, under increased voltage conditions, the excitation current is reduced to maintain stable operating parameters of the generating system.

The excitation control process forms a closed-loop regulation structure in which generator terminal voltage acts as the feedback signal for the excitation controller. Such a control structure allows continuous correction of excitation operating conditions according to changes in generator electromechanical parameters and wind operating modes [14]. The excitation control subsystem operates according to the closed-loop control principle in which the generator terminal voltage is continuously compared with the reference voltage value. The resulting voltage error signal is processed by the excitation controller to generate the required excitation current correction signal. According to PID-based control principles, the proportional component provides fast response to voltage deviations, the integral component reduces steady-state regulation error, and the derivative component improves transient operating performance and damping characteristics [15].

The proposed excitation control approach is focused on minimizing voltage deviations and improving transient operating performance of the generating system during wind speed disturbances. The controller continuously adjusts the excitation current in order to reduce dynamic voltage oscillations, improve response speed, and maintain stable generator terminal voltage under variable operating conditions. Particular attention is given to reducing steady-state regulation error and improving stability of the generating system during rapidly changing wind modes. The application of PID-based excitation current regulation allows the generating system to dynamically compensate voltage deviations caused by continuously changing wind conditions and improve voltage stabilization performance under transient operating modes. In the proposed wind energy conversion system, excitation current regulation is used not only for voltage stabilization but also for improving the dynamic operating performance and operational efficiency of the generating system under variable wind speed conditions.

3.2. PI/PID-Based Control Algorithm

The proposed excitation control algorithm is developed for stabilization of synchronous generator operating conditions under variable wind speed modes in a small-scale wind energy conversion system. The control approach is based on continuous regulation of the excitation current according to generator terminal voltage deviations and dynamic operating conditions of the generating system.

In the proposed control structure, the generator terminal voltage is continuously measured and compared with the predefined reference voltage value. The resulting voltage deviation signal is used as the input parameter for the excitation controller. According to the developed control logic, the excitation subsystem dynamically adjusts the excitation current in order to compensate voltage deviations caused by fluctuations of wind speed and mechanical loading conditions.

The developed excitation control algorithm employs a PID-based regulation structure due to its relatively simple implementation, high operational reliability, and effective dynamic response characteristics under continuously changing operating conditions [16]. The proportional component of the controller provides rapid response to voltage deviations, the integral component minimizes steady-state regulation error, and the derivative component improves damping characteristics and transient operating stability of the generating system.

The proposed control algorithm operates according to a closed-loop excitation current regulation principle. Under decreasing generator terminal voltage conditions, the controller increases excitation current supplied to the rotor winding in order to strengthen the magnetic field and compensate voltage reduction. Conversely, under increasing voltage conditions, the excitation current is reduced to maintain stable operating characteristics of the synchronous generator.

Unlike conventional fixed-excitation operating modes, the proposed excitation regulation approach provides continuous adaptation of generator electromagnetic operating parameters according to changing wind conditions. Such an operating principle improves voltage stabilization performance and reduces the influence of transient wind disturbances on generator operating conditions [17].

In the developed control structure, excitation current is used as the main control parameter of the synchronous generator operating process. The application of excitation-current-based regulation allows stabilization of generator terminal voltage without the need for complicated converter structures and high-power control equipment. Such an approach is especially important for small-scale wind energy systems where system simplicity, operational reliability, and reduced control complexity are significant engineering requirements [18].

The proposed excitation control algorithm is intended for implementation in the MATLAB/Simulink environment for further investigation of voltage stabilization characteristics and dynamic operating performance of the generating system under variable wind speed conditions.

3.3. Control Structure under Variable Wind Speed Conditions

The operating performance of the developed wind energy conversion system is strongly influenced by continuously changing wind speed conditions causing dynamic variations of turbine rotational speed, mechanical torque, and synchronous generator operating parameters. Under such operating conditions, the excitation control subsystem continuously adapts the generator excitation current in order to maintain stable voltage characteristics and improve operating stability of the generating system.

The proposed control system operates according to a closed-loop voltage stabilization principle. During generator operation, the terminal voltage is continuously monitored and compared with the predefined reference voltage value. Variations caused by wind speed disturbances or changing loading conditions produce a voltage deviation signal that is processed by the excitation controller. Based

on the generated control signal, the excitation subsystem dynamically adjusts the excitation current supplied to the rotor winding of the synchronous generator.

Under increasing wind speed conditions, the mechanical power transmitted to the generator increases, causing changes in generator electromagnetic operating parameters and terminal voltage characteristics. In such operating modes, the proposed control algorithm performs continuous correction of excitation current in order to prevent excessive voltage deviations and maintain stable operating conditions of the generating system.

Under decreasing wind speed conditions, generator terminal voltage may decrease due to reduction of mechanical torque and generator rotational speed. In this case, the excitation controller increases the excitation current to strengthen the rotor magnetic field and compensate voltage reduction. Such an operating principle improves voltage stabilization performance and reduces the influence of transient wind disturbances on generator operating conditions.

The proposed control system continuously adapts excitation operating parameters according to changing electromechanical operating modes of the synchronous generator. The closed-loop excitation regulation structure provides improved dynamic response characteristics and reduces steady-state voltage regulation error under variable wind speed conditions [19].

Particular attention in the developed control approach is given to stabilization of transient operating performance during rapidly changing wind conditions. The proposed excitation control logic allows reduction of dynamic voltage oscillations and improves damping characteristics of the generating system under electromechanical disturbances. Continuous excitation current correction also improves operational stability of the synchronous generator during variable mechanical loading modes [20].

The developed operating logic of the excitation control system forms the basis for further simulation studies of voltage stabilization characteristics and dynamic operating behavior of the proposed wind energy conversion system in the MATLAB/Simulink environment.

4. MATLAB/Simulink Modeling and Dynamic Analysis

4.1. MATLAB/Simulink Model of the Proposed Wind Energy Conversion System

The developed wind energy conversion system was implemented in the MATLAB/Simulink environment using a subsystem-based modeling approach for investigation of aerodynamic and electromechanical operating processes in a small-scale wind energy conversion system [21]. The proposed simulation model includes interconnected subsystems representing the wind turbine, aerodynamic conversion process, and synchronous generator operating subsystem.

Figure 2 presents the general MATLAB/Simulink structure of the proposed wind energy conversion system. The developed model consists of aerodynamic and electrical subsystems interconnected through the electromechanical energy conversion process. Mechanical power generated by the wind turbine subsystem is transferred to the synchronous generator subsystem, where electrical energy conversion and operating parameter calculations are performed. The developed model structure enables investigation of voltage characteristics, generated power, rotational speed behavior, and dynamic operating response of the system under variable wind conditions.

The wind turbine aerodynamic subsystem shown in Figure 3. performs calculation of the main aerodynamic operating parameters of the wind energy conversion system. The subsystem determines the mechanical power and mechanical torque generated by the wind turbine according to wind speed, turbine rotational speed, and aerodynamic operating conditions. The developed subsystem structure enables investigation of transient aerodynamic operating behavior under changing wind conditions and variable turbine operating modes.

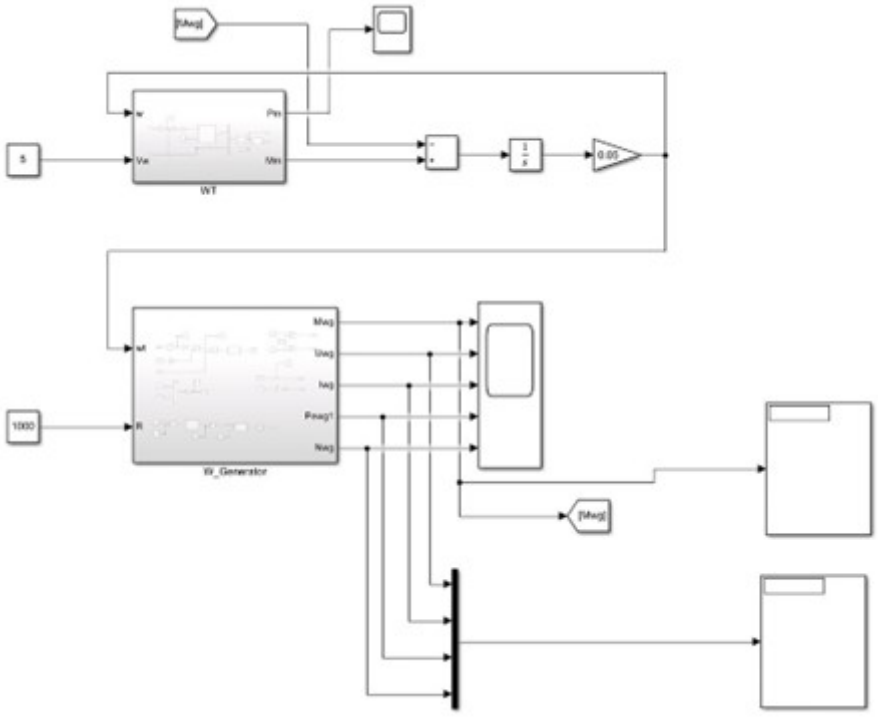

Figure 2 – General MATLAB/Simulink model of the proposed wind energy conversion system

The aerodynamic efficiency of the wind turbine is determined according to the aerodynamic power coefficient $C_p(\lambda, \beta)$, which depends on the tip-speed ratio λ and blade pitch angle β. The corresponding aerodynamic power coefficient subsystem is discussed in subsection 4.2.

The electrical energy conversion process is performed by the synchronous generator subsystem, which calculates the main electrical operating parameters of the generating system. The corresponding synchronous generator subsystem model and dynamic electrical operating characteristics are discussed in subsection 4.3.

The developed MATLAB/Simulink model provides an integrated simulation platform for further investigation of dynamic operating characteristics and voltage stabilization processes in the proposed wind energy conversion system. The subsystem-based structure of the model also enables implementation and investigation of excitation-current-based control approaches under variable wind operating conditions [22].

4.2. Simulation Parameters and Operating Conditions

The simulation studies of the proposed wind energy conversion system were performed in the MATLAB/Simulink environment under variable aerodynamic and electromechanical operating conditions in order to investigate the dynamic operating behavior of the generating system [23]. Particular attention was given to investigation of voltage characteristics, generated electrical power, and rotational speed response under changing wind operating modes.

The aerodynamic operating characteristics of the wind turbine were determined according to the aerodynamic power coefficient $C_p(\lambda, \beta)$, which depends on the tip-speed ratio λ and blade pitch angle β. Figure 4 presents the developed aerodynamic power coefficient subsystem implemented in the MATLAB/Simulink environment. The subsystem performs nonlinear calculation of aerodynamic operating efficiency according to changing turbine operating conditions and wind speed variations.

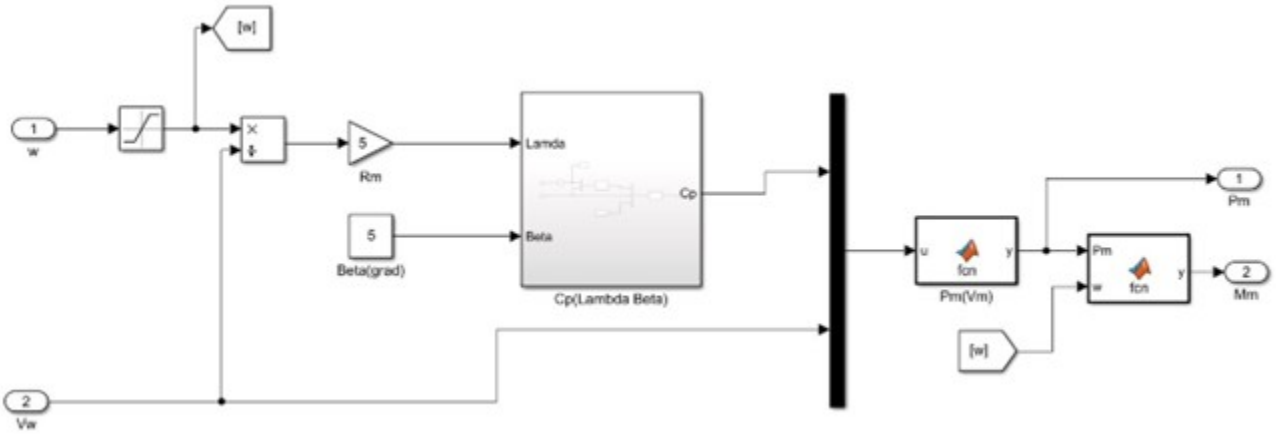

Figure 3 – Wind turbine aerodynamic subsystem model

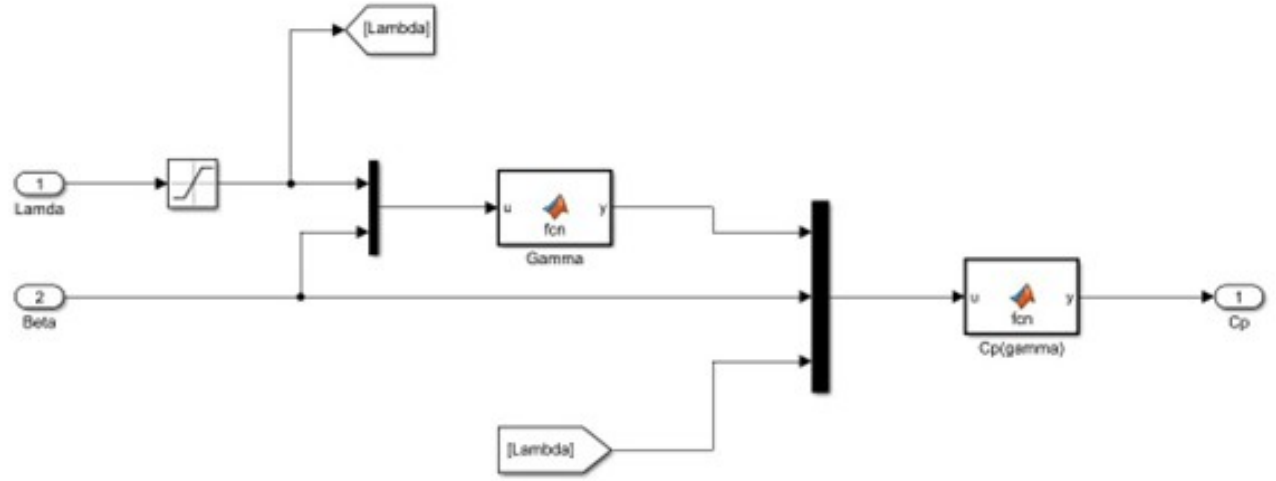

Figure 4 – Aerodynamic power coefficient subsystem Cp (λ, β)

The aerodynamic power extracted from the wind flow was determined according to the wind turbine power relationship presented in 1, where the aerodynamic power coefficient depends on the tip-speed ratio and blade pitch angle [23].

During the simulation process, variable wind speed conditions were applied in order to investigate transient operating characteristics of the wind energy conversion system under changing aerodynamic operating modes. The blade pitch angle β was considered constant during the simulation studies, while the tip-speed ratio λ varied according to turbine rotational speed and wind velocity changes.

The developed simulation model also included operating parameters associated with the synchronous generator, including generated voltage, electrical power, and rotational speed characteristics. The simulation conditions enabled investigation of the interaction between aerodynamic operating processes and electrical energy conversion under transient wind disturbances.

The MATLAB/Simulink simulation environment provided the possibility for dynamic investigation of operating stability and voltage stabilization characteristics of the proposed wind energy conversion system under variable wind conditions.

4.3. Dynamic Operating Characteristics of the Proposed WECS

The dynamic operating characteristics of the proposed wind energy conversion system were investigated using the developed MATLAB/Simulink model under variable wind operating conditions. Particular attention was given to the analysis of transient voltage response, electromechanical operating stability, and the influence of excitation-current regulation on the dynamic behavior of the synchronous generator subsystem [24].

Figure 5. presents the developed synchronous generator subsystem implemented in the MATLAB/Simulink environment. The subsystem performs calculation of generated voltage, electrical power, generated current, and rotor rotational speed during transient operating conditions. The developed model structure enables investigation of the electromechanical interaction between aerodynamic power variation and electrical energy conversion processes in the generating system.

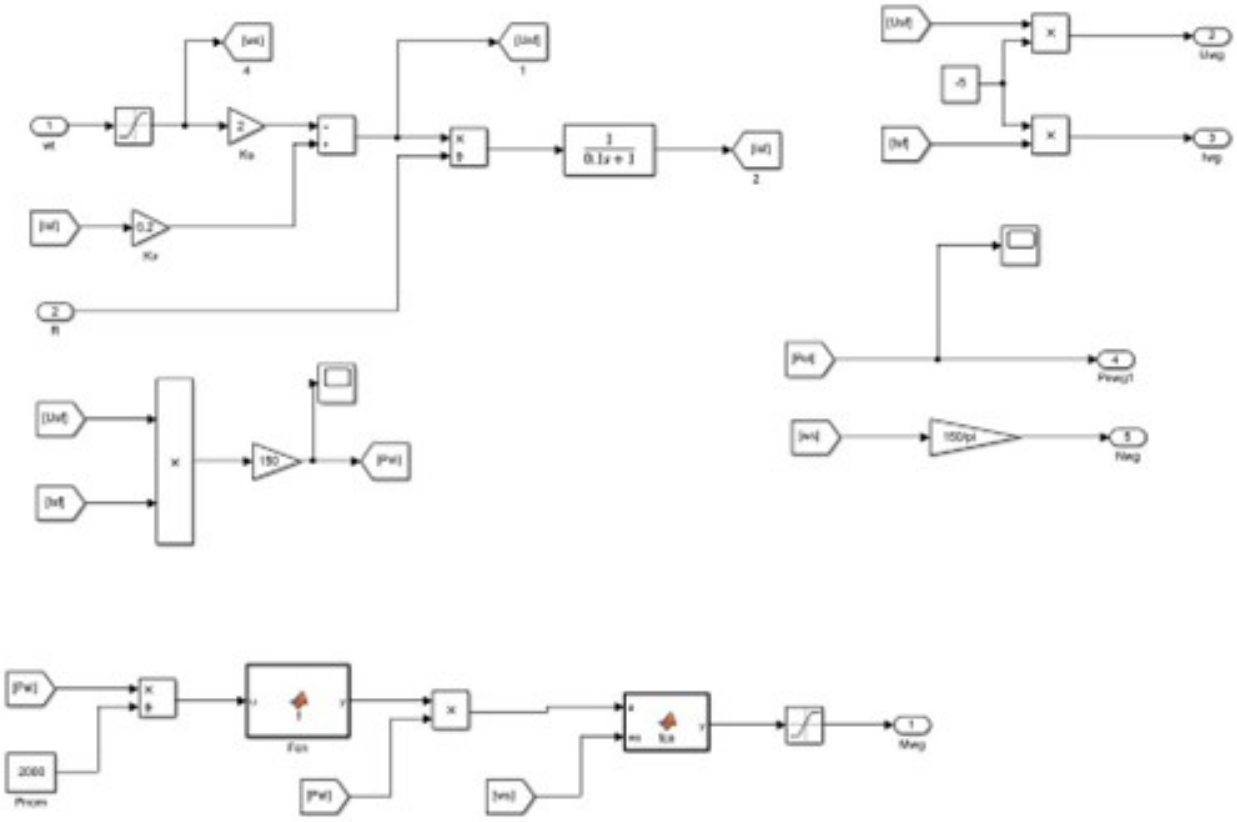

Figure 5 – Synchronous generator electrical subsystem model

Under variable wind speed conditions, fluctuations of aerodynamic input power produce corresponding variations in turbine mechanical torque and rotor rotational speed. These disturbances directly affect the electromagnetic operating state of the synchronous generator and may lead to transient voltage deviations and oscillatory operating behavior during rapidly changing wind conditions. The transient voltage response of the proposed wind energy conversion system obtained during simulation studies is presented in Figure 6. The simulation results demonstrate the dynamic voltage stabilization characteristics of the synchronous generator subsystem under changing wind operating conditions.

Figure 6. shows that transient changes in aerodynamic input power produce corresponding voltage deviations and oscillatory electromechanical response of the generating system. During rapidly

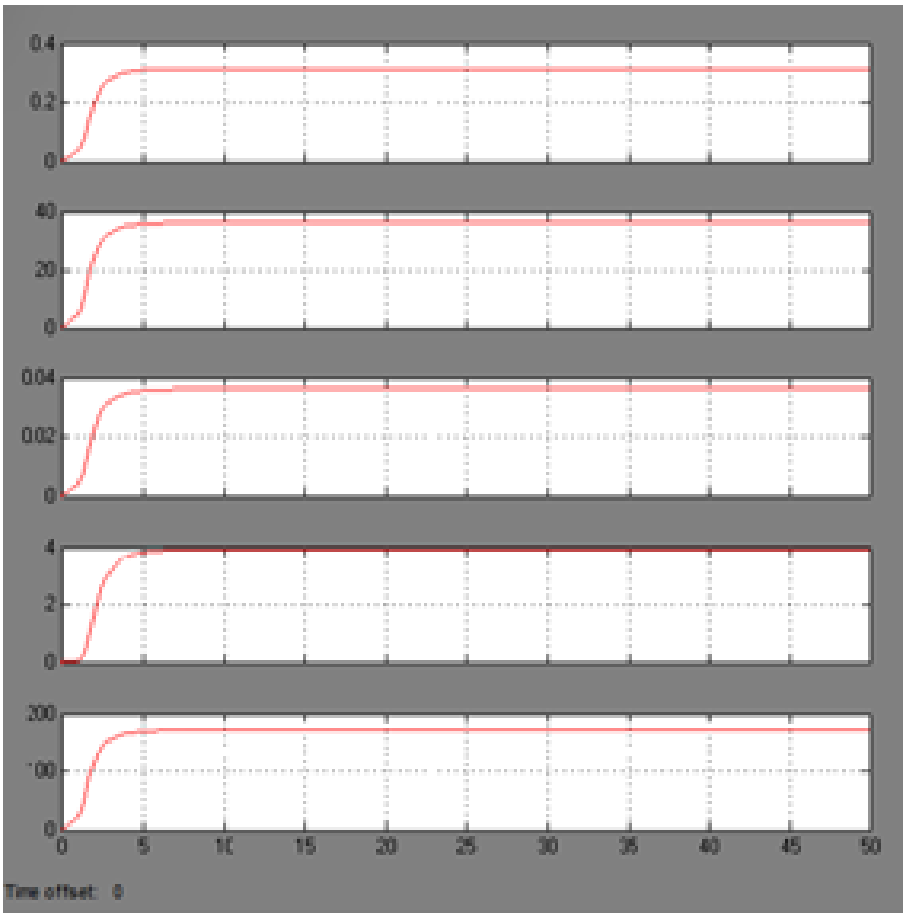

Figure 6 – Generator terminal voltage response under transient wind operating conditions

changing wind operating modes, imbalance between turbine mechanical power and generator electromagnetic operating conditions causes temporary voltage instability and dynamic disturbances in the synchronous generator subsystem.

The obtained simulation results demonstrated that excitation-current regulation improves voltage stabilization performance and enhances the transient operating response of the generating system. Continuous adjustment of excitation current enabled dynamic compensation of voltage deviations caused by variations in turbine rotational speed and aerodynamic power fluctuations. As a result, the proposed excitation control structure reduced transient voltage oscillations and improved damping characteristics during electromechanical disturbances.

The performed simulation analysis confirmed that excitation-current-based regulation improves adaptation of the synchronous generator to variable mechanical operating conditions and enhances operating stability under stochastic wind disturbances. The developed MATLAB/Simulink model can therefore be effectively used for investigation of transient electromechanical processes and dynamic voltage stabilization characteristics in small-scale wind energy conversion systems.

4.4. Analysis of Voltage Stabilization Performance

Analysis of the simulation results demonstrated that the operating characteristics of the proposed wind energy conversion system strongly depend on the interaction between aerodynamic operating conditions and synchronous generator electromechanical response. Variations in wind speed directly influence turbine rotational speed, generated electrical power, excitation current, and voltage stabi-

lization characteristics of the generating system.

The generated power characteristics of the proposed wind energy conversion system under different wind speed conditions are presented in Figure 7. The obtained simulation results demonstrate the nonlinear relationship between turbine rotational speed and generated electrical power under changing aerodynamic operating modes.

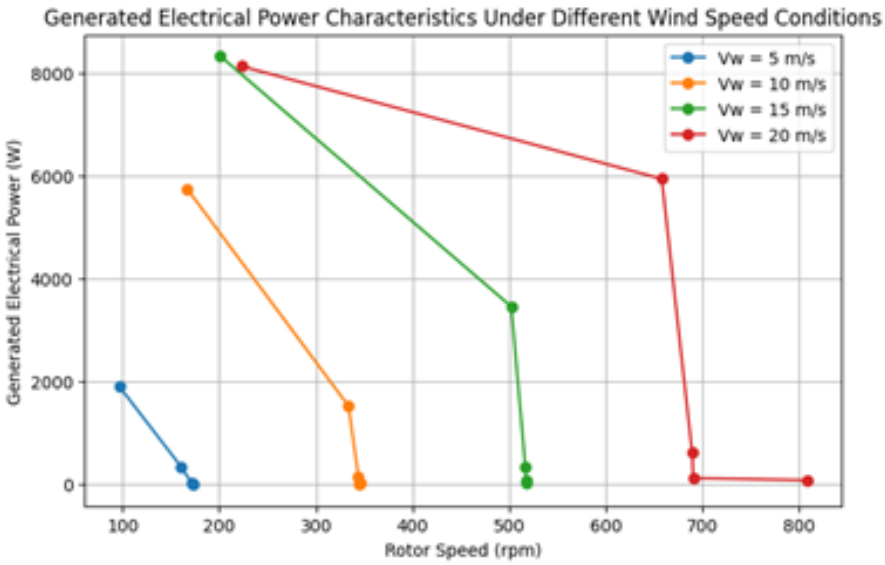

Figure 7 – Generated electrical power characteristics under different wind speed conditions

As shown in Figure 7, increasing wind speed significantly affects the generated electrical power and operating range of the wind energy conversion system. Under higher wind speed conditions, the turbine produces increased mechanical power, resulting in higher generator rotational speed and increased electrical power generation. The obtained characteristics also demonstrate the strong dependence of generated electrical power on aerodynamic operating conditions and turbine rotational speed variation.

The main simulation results of the proposed wind energy conversion system obtained under different wind speed and loading conditions are presented in Table 1.

The obtained simulation data demonstrate that variations in wind speed and electrical loading conditions significantly influence generator voltage, excitation current, generated electrical power, and rotor rotational speed characteristics. Under increased wind speed conditions, the generated electrical power and generator voltage increase due to higher aerodynamic input power transmitted to the synchronous generator subsystem.

The performed simulation analysis also showed that electrical loading conditions strongly affect the electromechanical operating characteristics of the generating system. Under reduced load resistance conditions, the generated electrical power increases while rotor rotational speed decreases due to increased electromagnetic loading of the synchronous generator. At the same time, excitation-current regulation improves stabilization of generator operating parameters and reduces the influence of transient aerodynamic disturbances on voltage response characteristics.

The obtained results confirm that excitation-current-based regulation represents an effective approach for improving voltage stabilization performance and operating efficiency of small-scale wind energy conversion systems under variable wind operating conditions. The developed MATLAB/Simulink model can therefore be effectively used for further investigation of advanced excitation control approaches and adaptive operating strategies for distributed renewable energy systems.

Table 1. Simulation results under different wind speed conditions

R	U_{sf}	I_{sf}	P_{el}	n_{wt}
V_w**, 5 m/s**				
1000	36,19	0,03618	3,94	172,6
500	35,98	0,07196	7,727	172,4
100	35,94	0,3594	38,74	171,2
10	34,56	3,563	351,9	160,3
1	24,25	24,25	1907	96,46
V_w**, 10 m/s**				
1000	72,34	0,07234	15,69	345,3
500	72,31	0,1446	31,37	346,1
100	72,16	0,7217	156,3	344
10	71,28	7,128	1526	333,8
1	43,83	43,83	5735	167,1
V_w**, 15 m/s**				
1000	108,5	0,1085	35,32	518
500	108,5	0,2169	70,6	517,8
100	108,4	1,084	352,8	516,8
10	107,4	10,73	3457	502,3
1	52,66	52,66	8319	201,2
V_w**, 20 m/s**				
1000	169,5	0,1693	86,07	809
500	169,1	0,2893	125,6	690,6
100	144,7	1,447	628,2	689,5
10	140,6	14,07	5937	658,1
1	58,38	58,37	8124	223

5. CONCLUSION

This paper presented the development and investigation of an excitation-current-based control approach for improving voltage stabilization and operating performance of a small-scale wind energy conversion system operating under variable wind speed conditions. The proposed system was developed using a synchronous generator with regulated excitation integrated into a MATLAB/Simulink-based electromechanical simulation model intended for investigation of transient aerodynamic and electrical operating processes.

A subsystem-oriented mathematical and simulation model of the wind energy conversion system was developed, including aerodynamic power conversion, synchronous generator dynamics, excitation regulation, and electrical loading processes. The developed model enabled investigation of the interaction between aerodynamic disturbances, turbine mechanical operating conditions, and synchronous generator electromechanical response under variable wind operating modes.

The performed simulation studies demonstrated that variations in wind speed significantly affect generator terminal voltage, excitation current, generated electrical power, and rotor rotational speed characteristics. Under transient operating conditions, imbalance between aerodynamic input power and generator electromagnetic response causes voltage deviations and oscillatory electromechanical behavior, negatively influencing operating stability and energy conversion performance of the generating system.

To improve operating stability under such conditions, a PI/PID-based excitation-current control

algorithm was implemented for continuous regulation of the synchronous generator magnetic field according to generator terminal voltage deviations. The obtained simulation results confirmed that excitation-current regulation improves voltage stabilization characteristics, reduces transient voltage oscillations, and enhances damping performance of the generating system during rapidly changing wind operating modes.

The developed excitation-based regulation approach also improved adaptation of the synchronous generator to variable mechanical loading conditions and reduced the influence of aerodynamic disturbances on electromechanical operating behavior. In comparison with more complicated converter-based regulation structures, the proposed approach provides comparatively low control complexity while maintaining effective voltage stabilization performance in small-scale wind energy conversion systems.

The obtained results confirm that excitation-current-based regulation represents an effective and practically applicable approach for improving operating stability and energy conversion efficiency of distributed renewable energy systems operating under stochastic wind conditions. The developed MATLAB/Simulink model can be further used for investigation of adaptive, intelligent, and hybrid excitation control methods intended for improvement of transient response characteristics, voltage quality, and operating efficiency of autonomous wind energy conversion systems.

REFERENCES

1. Global Wind Energy Council. “Global wind report 2025.” *Brussels, Belgium: GWEC* (2025):
2. International Renewable Energy Agency (IRENA). *Renewable Capacity Statistics 2025*. Abu Dhabi, UAE: IRENA, 2025.
3. Sankalpa, K. D. C., M. A. R. M. Fernando, and N. K. Wickramaarachchi. “Wind energy technologies: A complete review of the technologies and optimization techniques in modern wind energy conversion systems.” *Sustainable Energy Technologies and Assessments* 60 (2024):
4. Global Wind Atlas, “Wind resource data for Kazakhstan.” Technical University of Denmark (DTU) and World Bank Group, Tech. Rep., 2025.
5. Manwell, J. F., J. G. McGowan, and A. L. Rogers. *Wind Energy Explained: Theory, Design and Application*. Chichester, UK: Wiley, 2009.
6. Burton, T., N. Jenkins, D. Sharpe, and E. Bossanyi. *Wind Energy Handbook*. Chichester, UK: Wiley, 2011.
7. Ackermann, T. *Wind Power in Power Systems*. Chichester, UK: Wiley, 2012.
8. Li, H. and Z. Chen. “Overview of different wind generator systems and their comparisons.” *IET Renewable Power Generation* 2, no. 2 (2008): 123–138.
9. Müller, S., M. Deicke, and R. W. De Doncker. “Doubly fed induction generator systems for wind turbines.” *IEEE Industry Applications Magazine* 8, no. 3 (2002): 26–33.
10. Mihet-Popa, L. and I. Boldea. “Variable speed wind turbines using induction generator.” *IEEE Transactions on Energy Conversion* 23, no. 1 (2008): 132–140.
11. *IEEE Recommended Practice for Excitation System Models for Power System Stability Studies*, IEEE Std. IEEE Std 421.5-2016, 2016.
12. Machowski, J., J. W. Bialek, and J. R. Bumby. “Excitation control system for use with synchronous generators.” *IEE Proceedings – Generation, Transmission and Distribution* 145, no. 5 (1998): 537–546.
13. Kundur, P. *Power System Stability and Control*. New York, NY, USA: McGraw-Hill, 1994.
14. Njiri, J. G. and D. Söffker. “State-of-the-art in wind turbine control: Trends and challenges.” *Renewable and Sustainable Energy Reviews* 60 (2016): 377–393.
15. Benyoucef, K., M. Tadjine, and M. Boudour. “Optimal control strategies for DFIG-based wind turbines.” *Energy Conversion and Management* 122 (2016): 423–431.
16. Bossanyi, E. A. “Control of variable speed wind turbines.” *Wind Energy* 3, no. 3 (2000): 149–163.
17. Mseddi, A., S. Le Ballois, H. Aloui, and L. Vido. “Robust control of a wind conversion system based on a hybrid excitation synchronous generator: A comparison between H_∞ and CRONE controllers.” *Mathematics and Computers*

in Simulation 158 (2019): 453–476.

18. Mseddi, A., B. Dhouib, M. A. Zdiri, Z. Alaas, O. Naifar, T. Guesmi, B. M. Alshammari, and K. Alqunun. "Exploring the potential of hybrid excitation synchronous generators in wind energy: A comprehensive analysis and overview." *Processes* 12, no. 6 (2024): 1186.
19. "Optimizing PID controller parameters in wind energy conversion systems." *EPJ Web of Conferences* (2025):
20. "Comparative performance analysis of PI and PID controller for synchronous generator under variable wind speed." *International Journal of Advanced Engineering and Management* (2024):
21. Jonkman, J., "Modeling of the UAE wind turbine for refinement of FAST_AD." National Renewable Energy Laboratory (NREL), Golden, Colorado, USA, Tech. Rep. NREL/TP-500-34755, Dec. 2003.
22. Wei, C., Z. Zhang, W. Qiao, and L. Qu, "Intelligent maximum power extraction control for wind energy conversion systems based on online Q-learning with function approximation." in *Proc. IEEE Energy Conversion Congress and Exposition (ECCE)*, Pittsburgh, PA, USA, 2014, 4911–4916.
23. "Maximizing wind turbine efficiency using MATLAB/Simulink with integrated PMSG and MPPT." *Results in Engineering* 24 (2025):
24. Blaabjerg, F., R. Teodorescu, M. Liserre, and A. V. Timbus. "Overview of control and grid synchronization for distributed power generation systems." *IEEE Transactions on Industrial Electronics* 53, no. 5 (2006): 1398–1409.

Information about authors

Felix Bulatbayev *– Candidate of Technical Sciences, Associate Professor, Dean of the Faculty of Energy, Automation and Telecommunications, Abylkas Saginov Karaganda Technical University, Karaganda, Kazakhstan, e-mail: f.bulatbayev@ktu.edu.kz,*

Yuliya Bulatbayeva *– PhD, Associate Professor, Department of Automation of Production Processes, Abylkas Saginov Karaganda Technical University, Karaganda, Kazakhstan, e-mail: yu.bulatbaeva@ktu.edu.kz.,*

Abylai Bolatov *– Master's Student, Department of Energy Systems, Abylkas Saginov Karaganda Technical University, Karaganda, Kazakhstan, e-mail: abylabolatov@gmail.com.*